https://doi.org/10.5194/egusphere-2026-3378
Preprint. Discussion started: 1 July 2026

A warm stagnant ocean leads to deep-ocean deoxygenation without widespread anoxia

Benjamin W. Anthonisz[1], David K. Hutchinson[1,2,3], Katrin J. Meissner[1], Samar Khatiwala[4], and Benoît Pasquier[1,2]

[1]Climate Change Research Centre, University of New South Wales Sydney, Australia
[2]Australian Centre for Excellence in Antarctic Science, University of New South Wales Sydney, Australia
[3]ARC Centre of Excellence for 21st Century Weather, University of New South Wales, Sydney, Australia
[4]School of International Liberal Studies, Waseda University, Tokyo, Japan

Correspondence: Benjamin W. Anthonisz (benw.anthonisz@gmail.com)

Abstract. The speed and magnitude of anthropogenic climate change is unprecedented in the last 66 million years. To understand the potential impacts of these changes we must look to past abrupt warming events in the Earth's history. Proxy evidence suggests that some rapid warming events in the Earth's past have resulted in highly stratified ocean states and Oceanic Anoxic Events (OAEs), when large parts of the ocean became oxygen depleted and resulted in elevated extinction rates. Earth System Models (ESMs) typically struggle to represent highly stratified equilibrium states. Here we present three simulations under Miocene Climatic Optimum boundary conditions (MCO, ∼16.9-14.7 million years ago; Ma) with three different pCO_2 (1×, 2× or 3× preindustrial (PI)) using the Australian Earth System model (ACCESS-ESM1.5). When pCO_2 was raised to 2× or 3× PI pCO_2, circulation became dramatically altered due to cold initial conditions, resulting in a temperature-driven stratification which was stable for over 2000 years of integration. We then used a novel spin-up technique known as Anderson Acceleration (AA) to efficiently equilibrate the ocean biogeochemical fields, allowing us to investigate the equilibrium biogeochemical response to a stratified ocean state. While our high-CO_2 MCO simulations are still in a transient state of deep ocean warming, which although not representative of MCO equilibrium, can give us some insight into equilibrium biogeochemistry, including dissolved oxygen, in a mostly stagnant abyssal ocean. Surprisingly, we do not find large scale deep anoxia or hypoxia due to a shoaling of the remineralisation depth.

1 Introduction

Sea surface temperature (SST) and ocean stratification are increasing and are projected to continue increasing due to anthropogenic climate change (Arias et al., 2021). Increased SST leads to less oxygen uptake at the surface of the ocean (Oschlies et al., 2017) and increased stratification leads to reduced transport of oxygenated waters to the deep ocean (Shepherd et al., 2017). These physical changes reduce oxygen supply, and as a consequence, the ocean has become less oxygenated overall (Arias et al., 2021) while oxygen deficient zones in the tropical Pacific have expanded (Stramma et al., 2008). Declining oxygen concentrations can change marine community structure, function, animal behaviour and cause mass mortality events (Breitburg et al., 2018). Continued deoxygenation of the ocean is therefore economically and ecologically important.

https://doi.org/10.5194/egusphere-2026-3378
Preprint. Discussion started: 1 July 2026

The Earth's ocean has undergone multiple Oceanic Anoxic Events (OAEs) in the past (Rampino et al., 2023; Gérard et al., 2025). These events are characterised by a high global fraction of benthic anoxia often associated with rapid changes in climate due to tectonic or volcanic activity (Rampino et al., 2023; Mancini et al., 2024), however their drivers are not fully understood (Gérard et al., 2025). There are two hypotheses for persistent anoxia at depth. One is the preservation hypothesis, where increased stratification prevents circulation of oxygenated waters and allows the formation of large areas of anoxic bottom waters, particularly where circulation is restricted by topographic barriers (Sooraj et al., 2024). The second is the productivity hypothesis, where increased biological activity and export production elevates oxygen demand and results in the formation of oxygen deficient zones (ODZs) and allows for the accumulation of organic matter that has not been consumed underneath them. OAEs are associated with ecological disruptions and elevated extinction rates in the fossil record (Rampino et al., 2023). A modern OAE would likely have irreversible consequences for marine ecosystems and the economic activity they support. Since OAEs are the result of a shifting balance between the supply and demand of oxygen, understanding the conditions for their formation requires tandem investigation of the ocean's physical and biogeochemical processes.

Many modern Earth System Models (ESMs) represent oceanic biogeochemical processes (e.g. Yool et al., 2020; Ziehn et al., 2020), enabling them to simulate oceanic oxygen concentrations. The representation of oceanic oxygen by ESMs has improved recently (Takano et al., 2023). Some ESMs from the Coupled Model Intercomparison Project phase 6 (CMIP6) have shown an improved ability to model de-oxygenation than their ocean-only component models (Takano et al., 2023), highlighting the importance of air-sea interactions in determining ocean oxygenation. One challenge in representing oceanic oxygen concentrations is the computational cost of integrating ESMs with biogeochemical (BGC) models to equilibrium, which may still have drifting oxygen concentrations after more than 1500 years of direct integration (e.g Duboc et al., 2024). Accelerating equilibration for the BGC sub-model can therefore reduce the computational cost of simulating and equilibrating biogeochemical processes. Here we use Anderson Acceleration (Anderson, 1965) to reduce the computational cost of integrating the BGC component of the Australian Earth System model (ACCESS-ESM1.5), allowing us to examine the equilibrium solution of ocean oxygen concentrations within a hypothetically stratified ocean under Miocene boundary conditions.

Anderson Acceleration (AA) is a form of sequence acceleration. It is a "black box" method, meaning it can be adapted to a model with relative ease (Khatiwala, 2023). AA treats the model simply as a function $\boldsymbol{g}(\boldsymbol{x})$ which takes a state x_k to a new state x_{k+1}. It defines a residual function $\boldsymbol{f}(\boldsymbol{x}) = \boldsymbol{g}(\boldsymbol{x}) - \boldsymbol{x}$ that represents the change between one state and the next, saves a set number of previous iterations and creates a new state by taking a weighted average of previous iterations. The weights are defined by a constrained least squares problem that minimises the residual function $\boldsymbol{f}(\boldsymbol{x})$ and for which the sum of all weights is normalised to 1 to ensure tracer conservation. In order to effectively accelerate biogeochemistry AA requires a repeating physical cycle. This means that the physical simulation is halted while AA is being used. A more complete mathematical description can be found in Appendix A1.

There are a range of different proxy estimates of atmospheric CO_2 concentration during the Miocene Climatic Optimum (MCO), depending on the type of proxy used (Rae et al., 2021; Steinthorsdottir et al., 2021b; Herbert et al., 2022). For example, terrestrial plant-based reconstructions using stomatal densities of leaf fossils have suggested around 450 ppm (Steinthorsdottir et al., 2021b), while some marine-based boron proxies suggest above 800 ppm (Rae et al., 2021). Thus, the MCO may have

https://doi.org/10.5194/egusphere-2026-3378
Preprint. Discussion started: 1 July 2026

an atmosphere corresponding to future climate change scenarios spanning from a mid-range emissions scenario such as the Shared Socio-Economic Pathway (SSP) 2-4.5 to a high range emissions scenario such as SSP3-7.0.

Simulations of the MCO with earth system models struggle to recreate the temperature patterns evidenced by proxies, with significant cold-biases in the high-latitudes (Burls et al., 2021), (Figure A1). Although simulations using higher concentrations (∼800 ppm) are typically closer to reconstructed temperatures, they fail to capture the weakened meridional temperature gradient reconstructed during the MCO: underestimating warming at the poles and overestimating warming in the tropics (Burls et al., 2021; Hossain et al., 2023). An inability to capture the meridional temperature gradient has major implications for ocean modelling. Deep water formation is strongly influenced by surface temperature and salinity in the high-latitudes, which are closely tied with large-scale temperature gradients.

The Miocene model intercomparison project (MioMIP1) simulations have found a wide range of possible meridional overturning circulation (MOC) modes between model (Naik et al., 2025). Of the 14 simulations studied in MioMIP1, 11 had Southern Ocean sinking (SMOC), of which six had North Atlantic sinking (AMOC), and three had North Pacific sinking (PMOC). Three simulations had no deep convection. Those simulations were set up with differing palaeographic boundary conditions (since the "MIP" was created after the experiments were run), hence some of the differences may be driven by different topography and ocean gateways.

Modelling studies comparing MCO circulation patterns under different paleo-bathymetry reconstructions have found that relatively small changes to seaways connecting the Arctic into the North Atlantic ocean can have a crucial influence on North Atlantic salinity balance, and hence the presence of an AMOC (Hutchinson et al., 2025; Liu et al., 2024) for which the difference in the amount of fresh water supplied to the Pacific vs the Atlantic appears to be a key control on the relative strength of the PMOC and AMOC (Naik et al., 2025). Furthermore, advection feedbacks between the Atlantic and Pacific can lead to a switching between PMOC and AMOC as a result of Arctic gateway changes (Hutchinson et al., 2025, 2019). Further, increased pCO_2 favours a reduced AMOC and strengthened PMOC (Hutchinson et al., 2025). This result partially aligns with a different MCO model study which found warmer initial conditions can weaken the AMOC while colder initial conditions can enhance the AMOC (Lee et al., 2025). Long-term Cenozoic proxy reconstructions of deep water formation in the middle Miocene have found some evidence of both PMOC and AMOC during this period, albeit both modes being somewhat uncertain (Ferreira et al., 2018).

Work directly comparing representations of temperature and circulation between models has found large differences in the representation of overturning and temperature gradients between models integrated under the same boundary conditions (Tan et al., 2026), and that ocean overturning modes simulated for the Miocene can be dependent on the initial conditions (Lee et al., 2025; Hutchinson et al., 2025). This implies that published results only represent one of multiple possible solutions for a given model. The dependency on initial conditions and the rate of change in boundary conditions is important to consider when using past changes to ocean circulation to understand modern changes to circulation under anthropogenic climate change. In the past circulation would have changed on geologic time scales whereas in the future changes may happen much faster (Drijfhout et al., 2025).

https://doi.org/10.5194/egusphere-2026-3378
Preprint. Discussion started: 1 July 2026

Here we present three simulations of the Miocene, using three different pCO_2 levels and constant paleo-bathymetry. Our two elevated pCO_2 simulations displayed almost no bottom water formation or ventilation of the ocean below 3000 m, most likely due to a "cold start" in their initialisation (i.e. deep ocean colder than equilibrium). This is in conflict with the proxy record that suggest sustained Southern Ocean deep water formation (Ferreira et al., 2018) and other simulations using similar boundary conditions, emphasising the impact of individual models and initialisation strategy on simulated MOC. Our stratified simulations do however provide an opportunity to test the preservation hypothesis of OAE formation in a highly stratified simulation using a relatively high resolution ESM.

2 Methods

We use the Australian Earth System Model, ACCESS-ESM1.5 (Ziehn et al., 2020). ACCESS-ESM1.5 uses the Modular Ocean Model 5.1 (MOM5) as its ocean sub-model. The World Ocean Model of Biogeochemistry And Trophic-dynamics (WOMBAT) is used for ocean biogeochemistry (BGC). ACCESS-ESM1.5's ocean has a horizontal grid of 300 by 360 cells with a 1° nominal resolution on a tripolar grid. Latitudinal resolution is not fixed and increases to 0.33° near the equator and $\sim$ 0.4° in the Southern Ocean. The ocean has 50 levels and a maximum depth of 6000 m. Vertical resolution is highest near the surface, the first 20 levels having a resolution of 10 m, while deeper levels gradually increase up to $\sim$ 300 m thickness. WOMBAT is a nutrient–phytoplankton-zooplankton–detritus model with 10 biogeochemical tracers, including oxygen and single functional types of phytoplankton, zooplankton and organic detritus (Oke et al., 2013).

All simulations were run with a fixed, prescribed atmospheric pCO_2. This allows us to specifically target a given level of CO_2, as indicated from paleo-proxy reconstructions, but allows the atmosphere to act as an inexhaustible reservoir of carbon.

We ran three MCO simulations: MC1, MC2 and MC3. These simulations use 1×, 2× or 3× PI CO_2 concentration (284.3 ppm) respectively to account for the uncertainty and range of atmospheric reconstructions (Steinthorsdottir et al., 2021a; Rae et al., 2021; Herbert et al., 2022) and to explore a wide range of plausible climates. The MCO was long enough ($\sim$1.8 million years; Steinthorsdottir et al., 2021a), that Earth's orbit cycled through a range of eccentricity, precession and obliquity levels. Orbital parameters are set to PI levels, in order to focus on the CO_2 and topography-driven changes in the MCO rather than orbital variability. Paleogeography for the MCO simulations was adapted from Burls et al. (2021). Notable differences between the paleogeography used and modern geography include a closed Bering Strait, an open Central American Seaway (CAS), land in place of the Barents Sea, and the Tethys Seaway (Figure 1). The initial physical conditions for the MCO simulations were taken from previous work simulating the MCO using a modified version of the coupled climate model Geophysical Fluid Dynamics Laboratory CM2.1 (referred to here as GFDL) described in Hutchinson et al. (2018), which was also simulated with 1×, 2× and 3× PI pCO_2 and the Burls et al. (2021) paleogeography (Hutchinson et al., 2025). The code and input files used to create the boundary conditions for the MCO simulation can be found at Hutchinson (2023). This resulted in a "cold start" initialisation, where the surface of the ocean heats faster than the deep ocean.

The spin-up procedure is shown in Figure 2. After initialisation from conditions taken from GFDL simulations of Hutchinson et al. (2025), the simulations were integrated for 1000 years without biogeochemistry. After 1000 years, initial BGC conditions

https://doi.org/10.5194/egusphere-2026-3378
Preprint. Discussion started: 1 July 2026

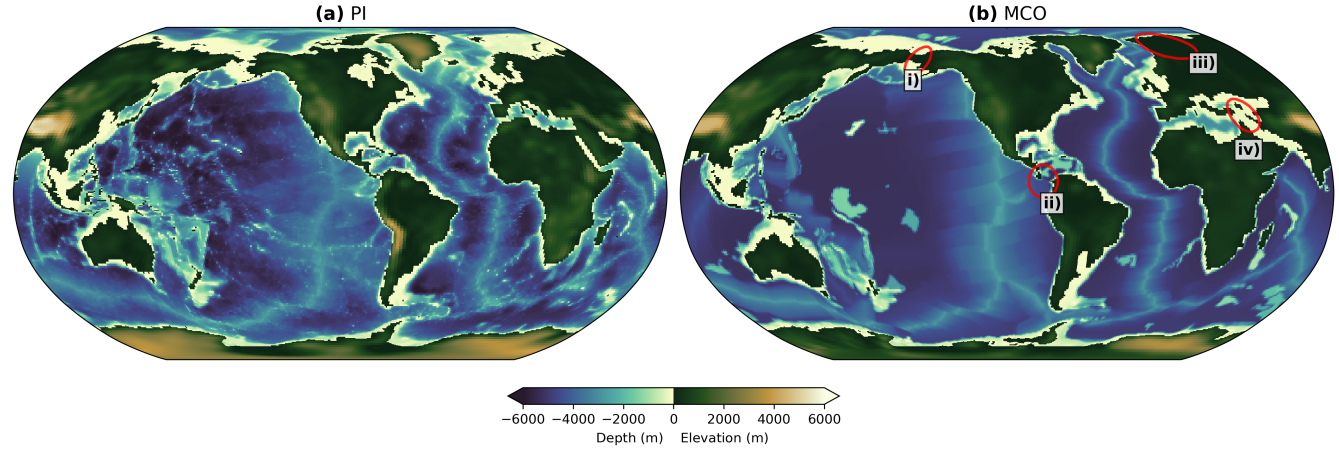

Figure 1. Bathymetry and topography of the (a) PI simulation and (b) MCO simulations. Key differences circled in red are: (i) closed Bering Strait, (ii) open Central American Seaway (CAS), (iii) land in place of the Barents Sea and (iv) the Tethys Sea and its connection to the Indian Ocean.

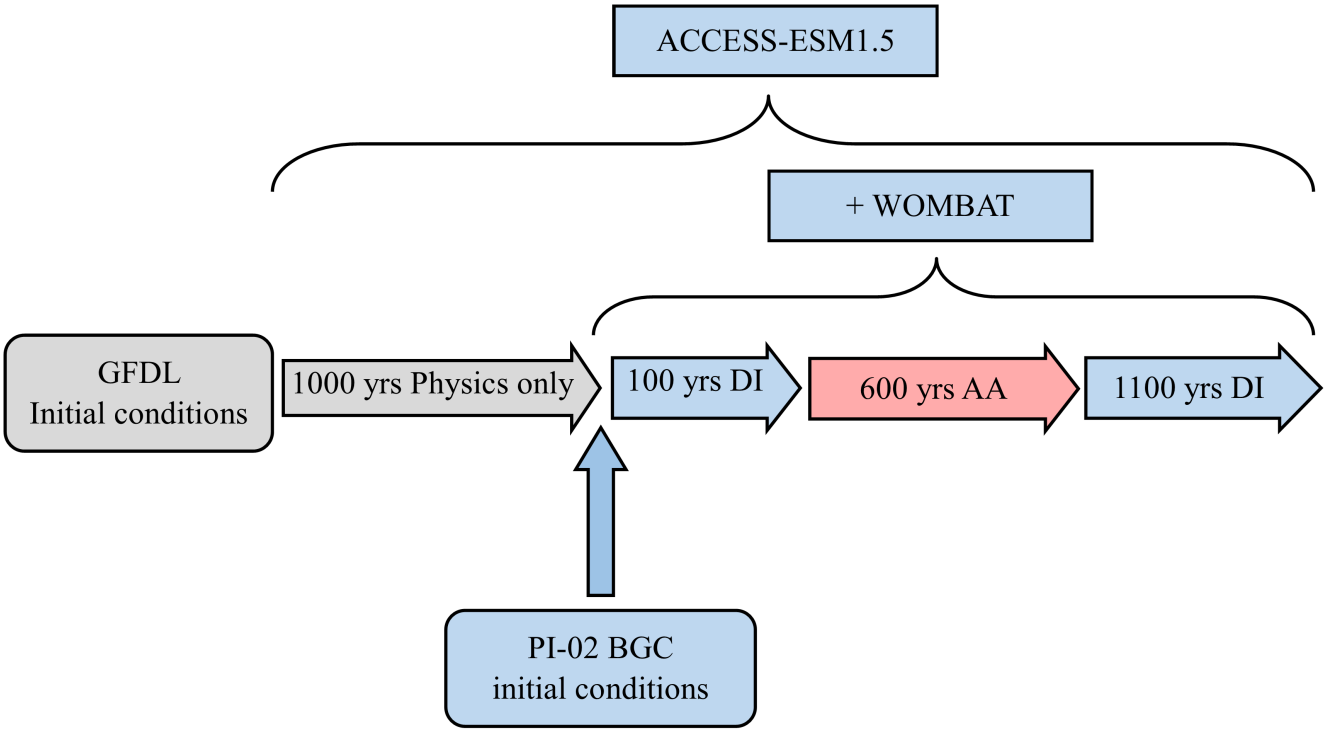

Figure 2. Experimental procedure for spinning up the Miocene Climatic Optimum simulations.

https://doi.org/10.5194/egusphere-2026-3378
Preprint. Discussion started: 1 July 2026

for WOMBAT were taken from the PI control run (PI-02 Mackallah et al., 2022) and interpolated to MCO paleo-bathymetry. Here we refer to conventional or online simulation of WOMBAT as "Direct Integration" (DI), to distinguish this from the AA-spinup phase. We first perform a 100 year spinup of WOMBAT using DI, followed by 600 years using AA. We used a cycle length of 10 years during the acceleration as a compromise between accounting for interannual variability and leveraging the acceleration algorithm. The fully coupled model was then integrated for a further 1100 years using DI, with the last 50 years being taken as the analysis period. The choices of simulation length were largely determined by computational constraints. We aimed to achieve a quasi-equilibrium because a full-equilibrium with zero drift was not feasible. The AA spinup enables the BGC model to reach an advanced state of equilibration, which is then allowed to evolve conventionally for long enough to identify any residual drifts. A more detailed description of our implementation of AA can be found in appendix A2.

3 Results

3.1 Spin-up

Table 1. Drift in average O_2 concentrations below 3000 m depth in mmol/m^3 per century averaged over the 100 years before AA, the 100 years after AA and the last 1000 years of direct integration.

Simulation	MC1	MC2	MC3
Before AA	-1.67	-3.11	-1.70
After AA	-0.131	-0.354	-0.509
Last 1000 years	$+0.830$	$+0.260$	-0.141

The combined spinup strategy of AA and DI produced an oxygen profile that is well equilibrated to the physical state of the simulation, even in water masses below 3000 m . There is much less drift in oxygen concentrations after the AA integration than before below 3000 m (Figure 3, Table 1). Changes to the oxygen profile after the AA integration are primarily driven by the subsequent changes in the physical simulation (which does not evolve during AA integration). The trend in oxygen concentrations below 3000 m in MC2 reverses towards the end of the DI integration (Figure 3b). MC2 shows increasing oxygen concentrations in waters associated with Antarctic Bottom Water (AABW) formation (Figure 3f), indicating a small increase in ventilation towards the end of the integration period. The increase in oxygen concentrations in North Pacific Intermediate Water (NPIW) (Figure 3d) for MC3 is due to strengthening NPIW formation over the course of the DI integration.

The ocean in all three simulations gains heat throughout their integrations (Figure 4), for MC2 and MC3, this trend shows no sign of equilibrating. As the deep ocean heats, the water column will eventually become unstable resulting in either: a slow restart of circulation, a fast restart (flush) due to instability, or a circulation that oscillates between off and on states on millennial scale frequency (Meissner et al., 2008).

https://doi.org/10.5194/egusphere-2026-3378
Preprint. Discussion started: 1 July 2026

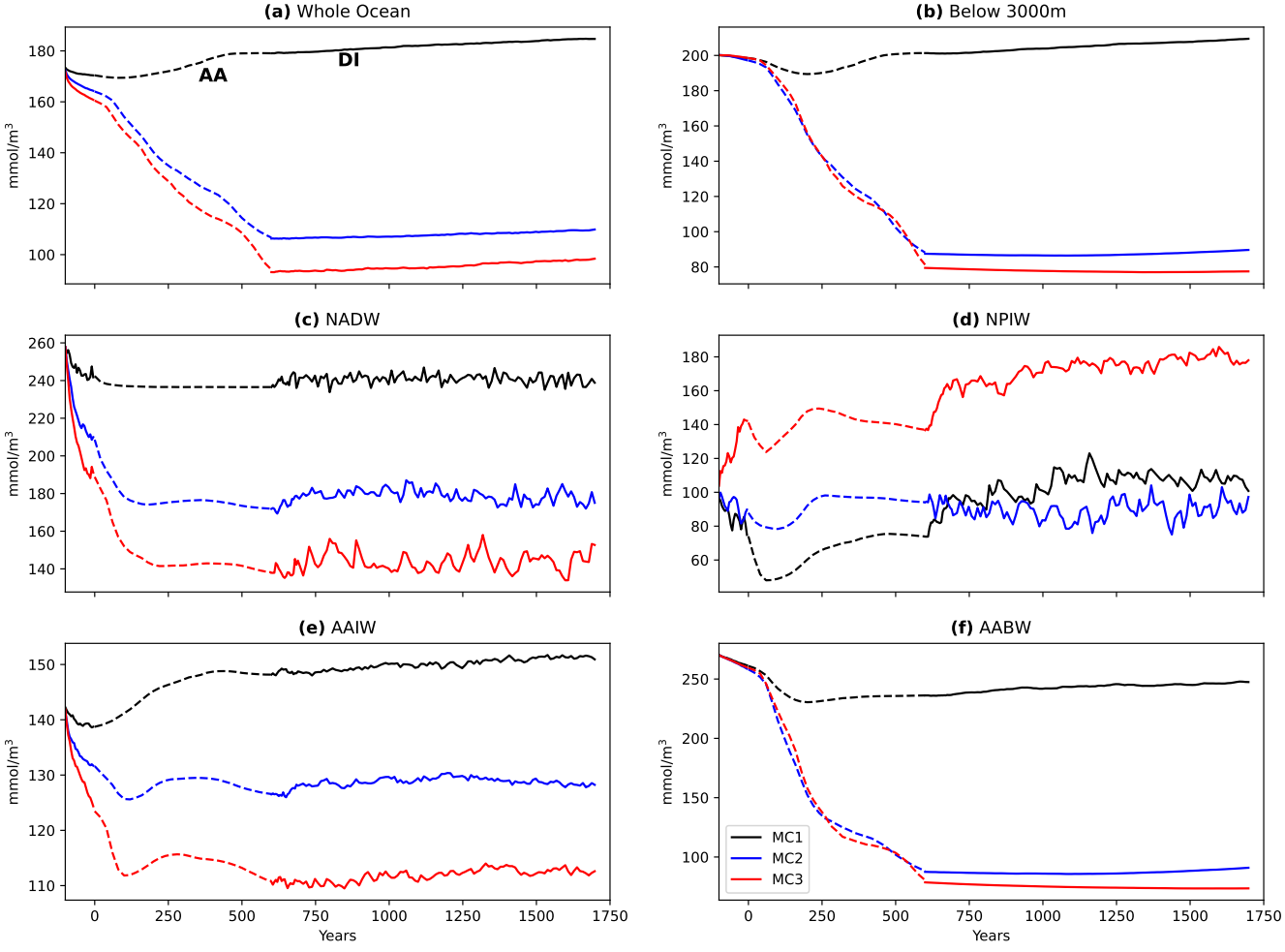

Figure 3. Time series of dissolved oxygen in MC1 (black), MC2 (blue) and MC3 (red) averaged for water masses: globally (a); below 3000 m (b); North Atlantic Deep Water (NADW), defined as Atlantic waters between 500 m and 1200 m depths, and 40°N to 60°N (c); North Pacific Intermediate Water (NPIW), defined as Pacific waters between 250 m and 1200 m depth, and 40°N to 60°N (d); Antarctic Intermediate Water (AAIW), defined as waters between 500 m and 1200 m depth, and 60°S to 10°N (e); and Antarctic Bottom Water (AABW), defined as waters below 4000 m depth and latitudes 60°S to 35°S (f). Year 0 is set as the year AA was engaged. Direct integration is shown with solid lines and Anderson acceleration integration with dashed lines.

Given the trending physical simulation, AA could have been engaged later to integrate biogeochemistry under better equilibrated physics, but with limitations in computational resources and time, engaging AA sooner saves time and allows for a longer post-AA integration to test the stability of the biogeochemical state produced. Uncertainty in how the physical simulation will evolve makes it difficult to optimise the spin up strategy *a priori*.

https://doi.org/10.5194/egusphere-2026-3378
Preprint. Discussion started: 1 July 2026

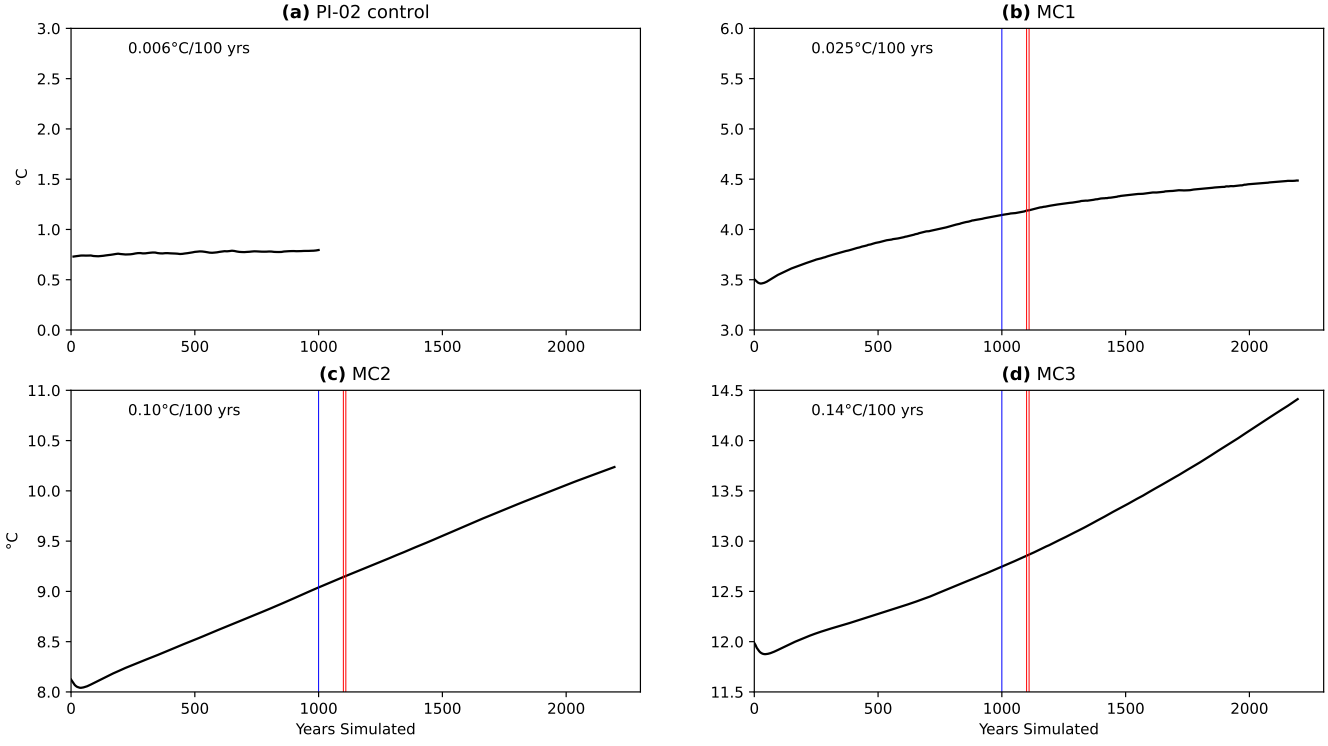

Figure 4. Average potential temperature in °C below 3000 m for the PI control simulation (a) and the three MCO simulations (b-d). Biogeochemistry switched on at year 1000 (blue line) in the MCO experiments. Anderson Acceleration physical cycle was from year 1100 to 1110 (red lines). Average potential temperature drifts over the last 1000 years of simulation are shown in the top left corner.

3.2 Ocean dynamics in MC1

Table 2. MOC, AMOC , PMOC, and SMOC for the simulations analysed in this study. To exclude wind driven circulation only values below 500 m for MOC, AMOC and PMOC and below 1000 m for SMOC were included.

Simulation	PI	MC1	MC2	MC3
MOC	22.9	19.6	14.1	22.9
AMOC	22.9	14.7	6.90	12.15
PMOC	4.3	6.85	3.86	8.39
SMOC	11.2	10.2	2.75	3.45

The MC1 simulation has globally increased near-surface air temperatures (SATs)and sea surface temperatures (SSTs) compared to PI (Figures A2, A3). The MC2 and MC3 simulations have increased SSTs and SATs compared with MC1, with the change being greater for the MC3 simulation (Figures A2, A3).

https://doi.org/10.5194/egusphere-2026-3378
Preprint. Discussion started: 1 July 2026

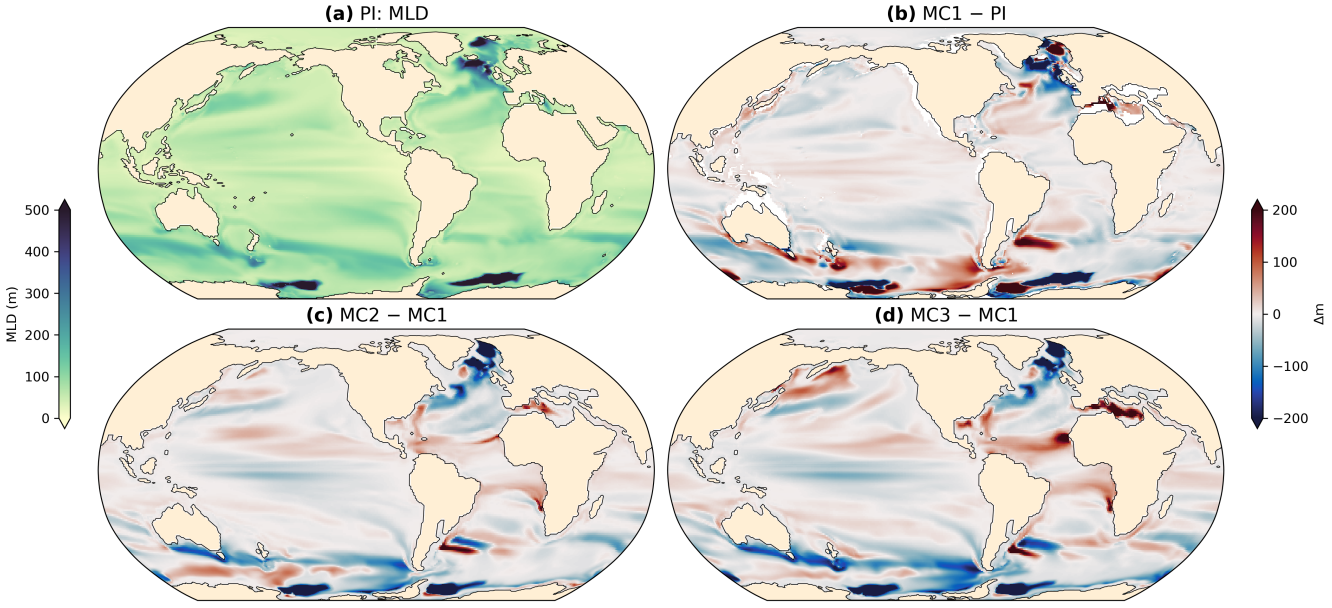

Figure 5. Mean mixed layer depth (MLD) averaged over the analysis period in m (a) for PI; MLD anomalies for (b) MC1 compared with PI, (c) MC2 compared with MC1 and (d) MC3 compared with MC1. Anomalies indicate a poleward shift of NADW and AABW formation sites in MC1, while in MC2 and MC3, there is a loss of AABW formation, weaker NADW formation and an enhancement of Tethys intermediate water formation.

MC1 retains recognisable ventilation sites and circulation patterns but with altered strength and locations. In ACCESS-ESM1.5, AABW is formed through open ocean convection (Yeung et al., 2024). AABW formation in the MC1 simulations is shifted towards the coast in both the Pacific and Atlantic sectors (Figure 5b) resulting in deep and bottom waters being better ventilated in the Ross and Weddell seas (Figure A4f). Northward advection of AABW is weaker in the MC1 simulation compared with the PI simulation, resulting in weaker ventilation north of formation sites (Figure A4f). North Atlantic Deep Water (NADW) formation sites also shift poleward in MC1 compared with PI (Figure 5a, 5b).

In the MC1 simulation, the upper overturning cell of the MOC is weaker than in the PI (Figure 6a, 6b, Table 2). The MC1 simulation features a concentrated maximum at $\sim 38^\circ$ N that is not present in the PI simulation (Figure 6a) and corresponds to circulation in the Tethys sea. The southern overturning cell extends further north (Figure 6a, 6b) but is slightly weaker at its maximum (Table 2).

In the Atlantic, the positive overturning cell of the AMOC is weaker and shallower in MC1 than in PI (Table 2, Figure 7). The streamfunction is not defined where there are open boundaries to the Atlantic (CAS and Tethys seaway). The upper cell of the AMOC becomes much weaker south of the CAS (thin grey bar at $\sim$ 12 °N, Figure 7b), indicating significant throughflow between the Pacific and Atlantic through the CAS. Water ages between 400 and 1400 m also suggest significant transport of younger waters from the Atlantic into the central Pacific via the CAS (Figure A4b). There is a slight increase in strength in the overturning circulation south of the boundary corresponding to the Strait of Gibraltar, implying that there is communication

https://doi.org/10.5194/egusphere-2026-3378
Preprint. Discussion started: 1 July 2026

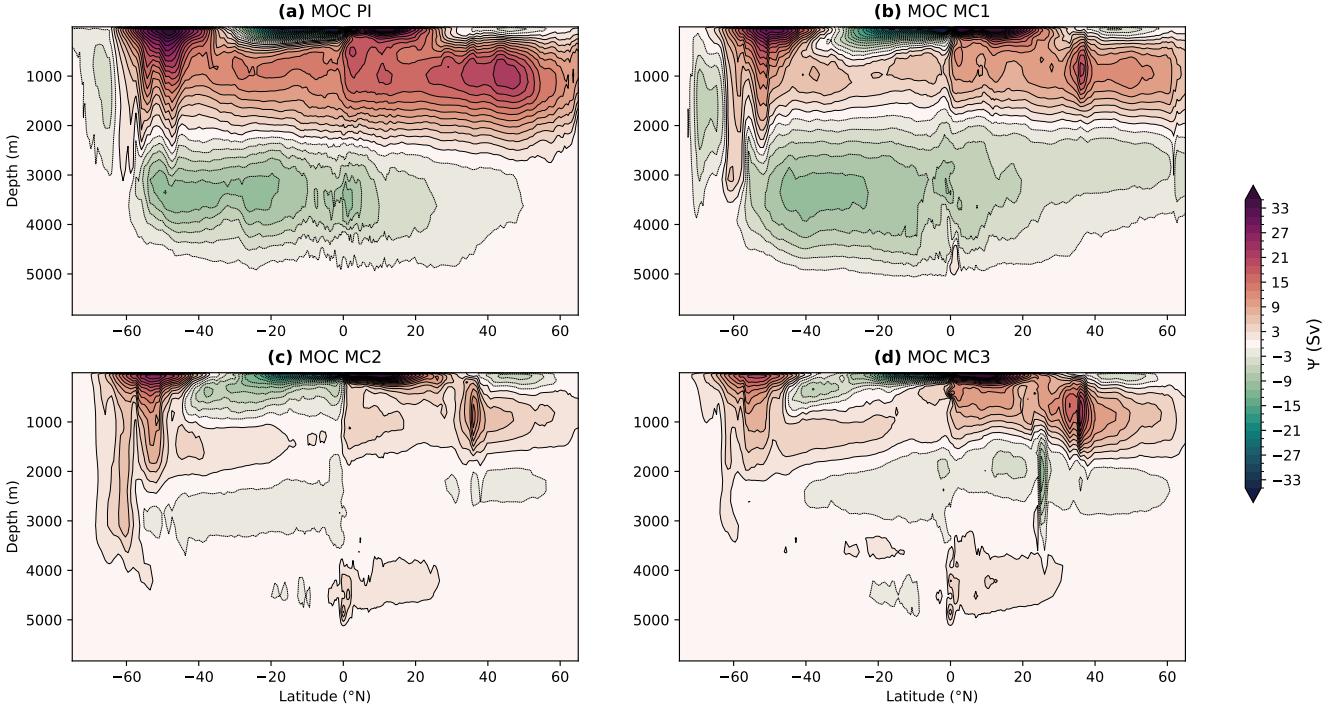

Figure 6. Streamfunction (Ψ) of zonally integrated meridional transport in Sverdrups (Sv, 10^6 m^3s^{-1}) to show Global Meridional Overturning (MOC) for (a) the PI control, (b) MC1, (c) MC2 and (d) MC3. The MOC is not shown in ACCESS-ESM1.5's tripolar grid region (north of 65° N).

between the Tethys and the Atlantic ocean (Figure 7b). The negative AMOC cell extends to shallower depths and is slightly stronger in MC1 compared to PI (Figure 7a, 7b).

In summary, MC1 shows deep water formation and circulation patterns with recognisable features of the PI simulation. There are key differences in strength and location of deep water formation, likely due to the increased temperatures in the MC1 simulation compared with PI (Figures A2, A3). MC1 retains an AMOC but with reduced strength and significant changes as a result of open seaways. MC1 has NADW and AABW formation, however the formation sites are moved poleward.

3.3 Ocean dynamics in MC2 and MC3

Deep water formation in the MC2 and MC3 simulations is substantially reorganised compared with the MC1 simulation. NADW formation in the MC2 and MC3 simulations is weaker than in MC1 (Figure 5) and is shifted southward, indicated by the maximum of the AMOC upper cell shifting southward (Figure 7). MC2 and MC3 do not feature AABW formation. There is still formation of dense waters and convection, but the water masses fail to reach the bottom of the ocean, resulting in the deep ocean being largely unventilated compared with the MC1 simulation (Figure 8h, 8l, 9h, 9l). The deepest monthly averaged mixed layer depth in the Ross and Weddell seas does not exceed 2000 m in the MC2 simulation and 1500 m in the

https://doi.org/10.5194/egusphere-2026-3378
Preprint. Discussion started: 1 July 2026

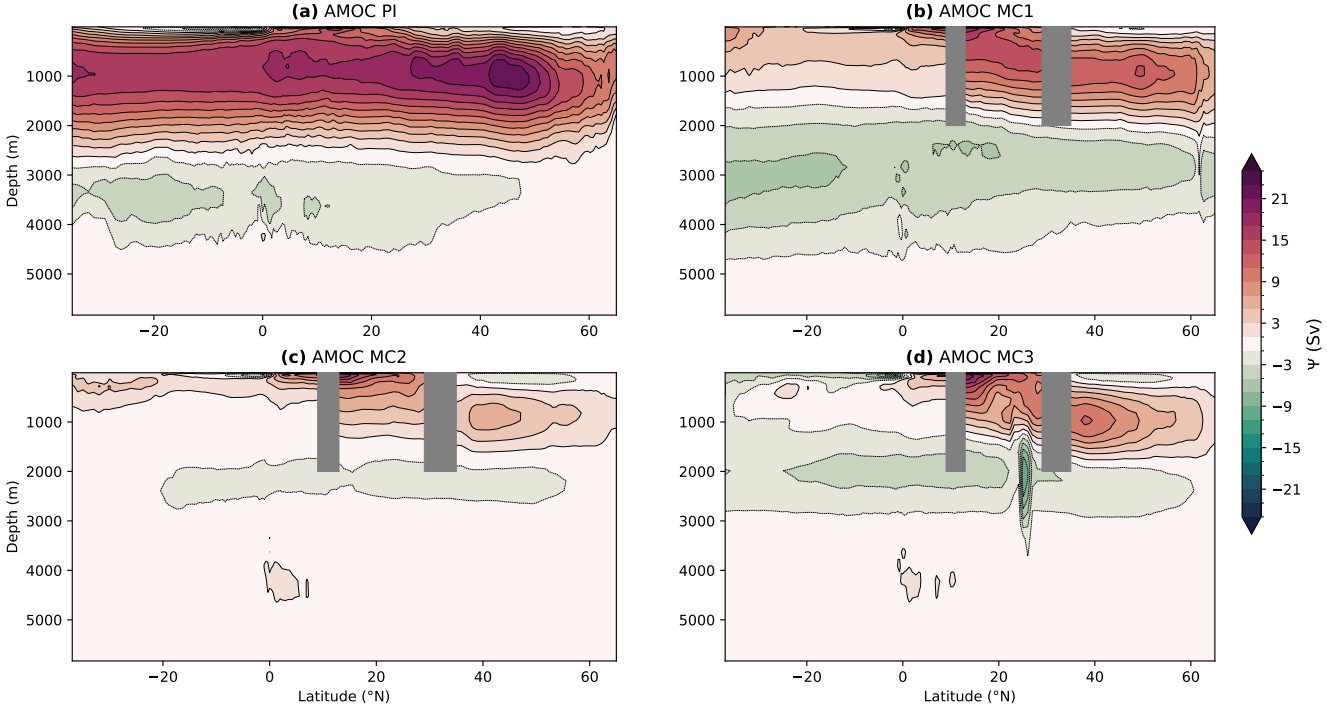

Figure 7. Streamfunction (Ψ) of zonally integrated meridional transport in Sverdrups (Sv, 10^6 m^3s^{-1}) to show the Atlantic Meridional Overturning (AMOC) for (a) the PI control, (b) MC1, (c) MC2 and (d) MC3. The latitudinal extent and depth of open boundaries for the Atlantic in the MCO (CAS and Tethys) are blocked out in grey, and the latitude range is restricted to exclude the open Southern Ocean and ACCESS-ESM1.5's tripolar grid region (north of 65° N).

MC3 simulation, compared with the MC1 simulations which has water mixing down to the ocean floor for every year in the analysis period (Figure A5).

The MC3 simulation exhibits salinity-driven bottom water formation in the Gulf of Mexico at 25°N (Figure A6), with increased mixed layer depths compared with the MC1 simulation (Figure 5). This mode of ventilation is intermittent: We use maximum monthly averaged MLD within the Gulf of Mexico to assess the temporal variability of this mode of ventilation and find it does not occur every year and is strongest in February (Figure A7). There is a similar but weaker mode of convection in the MC2 simulation (Figure A7). This bottom water remains mostly contained in the Gulf of Mexico (Figure A6).

The MCO simulations also feature deep water formation in the Tethys sea, especially the MC2 and MC3 simulations (Figure 5). This deep water formation is more consistent than that in the Gulf of Mexico, especially in the MC3 simulation (Figure A7 and A8).

MC2 and, to a greater extent, MC3 feature increased intermediate water formation off the west coast of Africa (Figure 5c, 5d), resulting in better ventilation in the tropical Atlantic above $\sim$ 1500 m (Figure 9h, 9l). The MC2 and to a greater extent

https://doi.org/10.5194/egusphere-2026-3378
Preprint. Discussion started: 1 July 2026

MC3 simulation have deeper mixed layers in the North Pacific compared with the MC1 simulation (Figure 5c, 5d) enhancing North Pacific ventilation above 2000 m in MC3 and 1400 m in MC2 (Figure 8h, 8l).

AABW formation ceases in the MC2 and MC3 simulations (Figures 5,6). The negative cell south of 60°S found in the PI and MC1 simulations is not present in either of the elevated pCO_2 simulations (Figure 6). High emissions experiments using ACCESS-ESM1.5 display a near identical loss of deep mixed layers in the Ross and Weddell seas and loss of the negative overturning cell south of 60°S. This shutdown in ventilation leads to the deep ocean becoming largely unventilated.

In the Atlantic, circulation is weaker in the MC3 and MC2 simulations than MC1. The positive maximum associated with Tethys overturning is still present in the MC2 and MC3 simulations, being strongest in the MC3 simulation (Figure 6). The lower negative overturning cell that is present in the MC1 simulation is much weaker in MC2 and does not extend as far south (Figure 7c). In the MC3 simulation, the lower negative cell extends further south and connects to the surface and is stronger than in MC2 but weaker than in MC1 (Figure 7d). MC3 features a strong negative minimum at 25 °N that is associated with salinity driven circulation in the Gulf of Mexico. The upper positive cell of the AMOC is weakest in MC2, slightly stronger in MC3, but both are weaker than MC1 and the PI (Table 2, Figure 7). Like in MC1 the upper positive cell is discontinuous at the latitudes of the CAS and the Tethys gateway, due to significant lateral flow through the gateways.

Increased NPIW formation in MC3 and intermediate water formation in the Atlantic and Tethys result in better ventilation above 1400 m in some sectors of the ocean for MC2 and most of the ocean for MC3 (Figure A4). In the MC2 and MC3 simulations, the deep ocean (below 2000 m) is exceptionally stagnant (Figures 8h, 8l, 9h, 9l, A4 bottom row). In the last year of the simulations, there is a significant number of grid boxes at the bottom of the ocean with water ages comparable to the length of the simulation (Figure A6), implying limited circulation in these water masses. Since the deep ocean continues to gain heat in the MC2 and MC3 simulations (Figure 4), it is possible that if physical integration continued, the ocean might at some point slowly regain deep and bottom water ventilation, or may "flush": where the water column becomes unstable and there is a rapid onset of circulation. Simulations representing OAEs using less complex models sometimes display oscillations in circulation, driving oscillations in oxygen concentrations with periods >1kyr (e.g Gérard et al., 2025) and flushes and oscillations on multi millennial time scales have been observed in other earth system models of intermediate complexity (e.g Meissner et al., 2008; Pohl et al., 2022; Zhu and Rose, 2025), however they are difficult to produce in a CMIP6 ESM such as ACCESS-ESM1.5 due to the multi-millennial timescales required to simulate them.

3.4 Oxygen

3.4.1 Oceanic Oxygen in the MC1 experiment

To isolate the impact of modified topography, the MC1 simulation is compared with the PI simulation. We use in situ O_2 concentration and saturated oxygen concentration (O_2^{sat}), which is the oxygen concentration that a parcel of water would be expected to have at the surface given the solubility of oxygen for its potential temperature and salinity. Comparing the O_2^{sat} concentration with O_2^{sat} gives apparent oxygen utilisation ($AOU = O_2 - O_2^{sat}$), an estimate of the amount of oxygen that appears to have been removed due to respiration. AOU is influenced by circulation (indicated here by water age), detritus

https://doi.org/10.5194/egusphere-2026-3378
Preprint. Discussion started: 1 July 2026

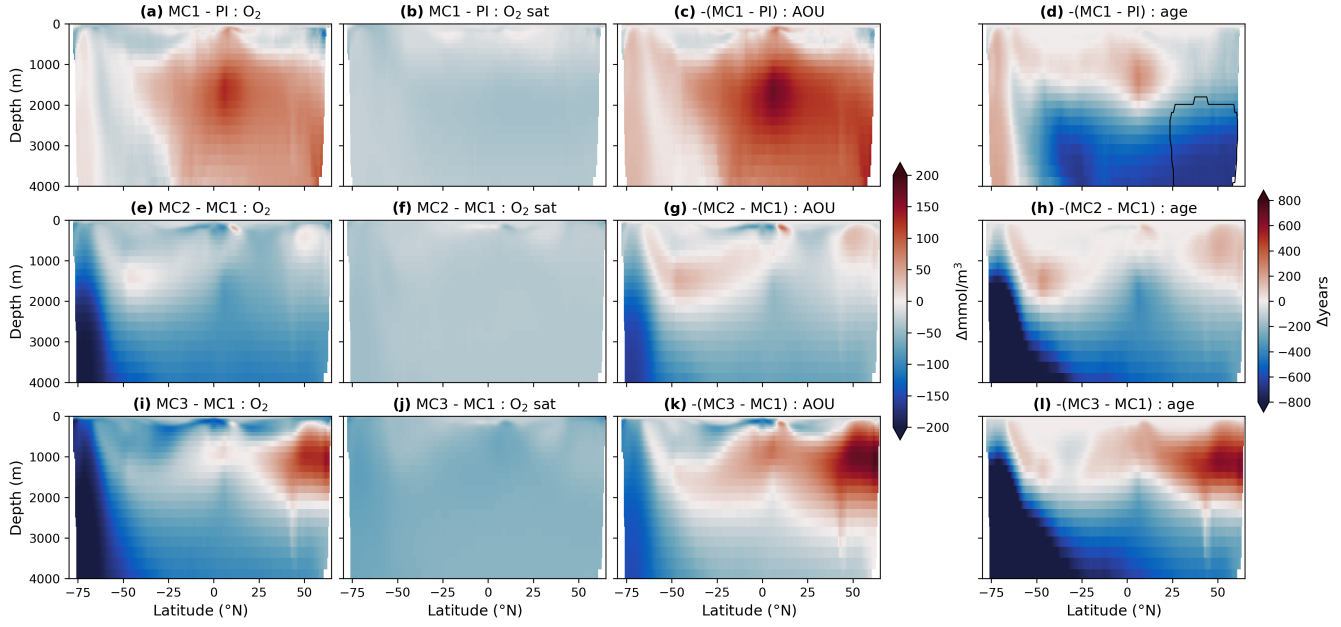

Figure 8. Anomalies of zonally averaged oxygen concentration (first column), O_{2sat} (second column), Apparent Oxygen Utilisation (AOU) $\times$-1 (third column) in mmol/m^{-3}, and water age $\times$-1 (last column) in years for the Pacific basin. Anomalies between MC1 and PI are shown in the first row, between MC2 and MC1 in the second row, and between MC3 and MC1 in the third row. Negative AOU and age anomalies have been plotted to show the direction of action on oxygen concentrations. The area enclosed by the black line in subplot d) was affected by an artificial age limiter in the PI control run, equilibrium age values are likely higher in this area.

concentrations and seawater temperature. Higher water age indicates more time for respiration to occur and respiration is proportional to detritus concentration and temperature in WOMBAT. As a result of the warmer surface in the MC1 simulation, zonally averaged O_2^{sat} decreases across the Pacific and Atlantic (Figure 8b, 9b). Despite this reduction in oxygen solubility, the MC1 simulation has higher globally averaged oxygen concentrations than the PI conditions it was initialised from (Figure 3a).

Oxygen concentrations increase over most of the Pacific compared to PI (Figure 8a). At depths above 1500 m and south of 25°N this change is partially attributable to increased circulation as a result of CAS through flow (indicated by reduced water age, Figure 8d) but in the North Pacific and at depth this is largely a result of reduced biological activity (indicated by reduced AOU, Figure 8c, and by reduced surface nutrients, Figure A9).

In the Atlantic, MC1 has generally lower oxygen concentrations that the PI simulation, with the exception of Antarctic Intermediate Water (AAIW) (Figure 9a) that is associated with reductions in age (Figure 9d) and AOU (Figure 9c). The reductions in oxygen can be primarily attributed to reductions in oxygen solubility (Figure 9). In the shallow tropical and subtropical North Atlantic there is an increase in AOU (Figure 9c) that is not associated with increased water age (Figure 9d). This increase in AOU is due to a significant increase in nutrients in shallow waters (Figure A9), leading to an increase in biological activity at the surface and an increase in export production (Figure A10d).

https://doi.org/10.5194/egusphere-2026-3378
Preprint. Discussion started: 1 July 2026

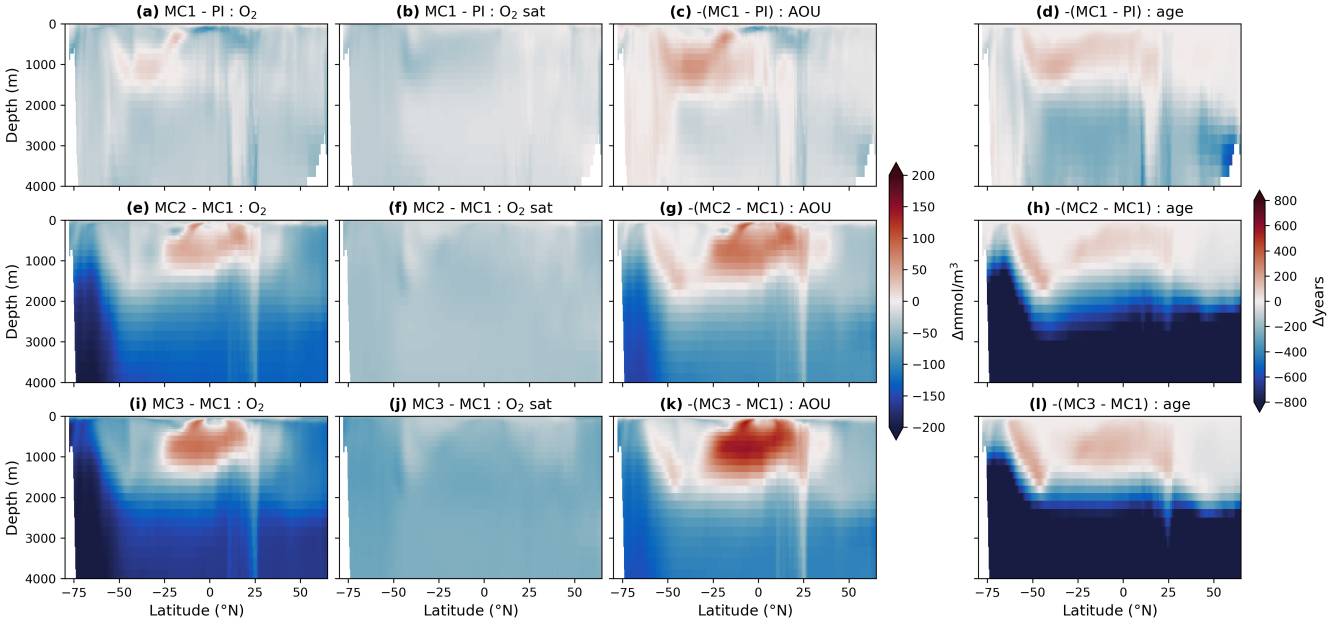

Figure 9. Anomalies of zonally averaged O_2 concentration (first column), O_{2sat} (second column), Apparent Oxygen Utilisation (AOU) $\times$-1 (third column) in mmol/m^{-3}, and water age $\times$-1 (last column) in years for the Atlantic basin. Anomalies between MC1 and PI are shown in the first row, between MC2 and MC1 in the second row, and between MC3 and MC1 in the third row. Negative AOU and age anomalies have been plotted to show the direction of action on oxygen concentrations.

To assess the impact of increased stratification and changed biogeochemistry on the deep ocean we examine bottom O_2 concentrations between simulations. The MC1 simulation has small negative anomalies in bottom oxygen concentration over almost all of the Atlantic, Indian and Southern Ocean (Figure 10b). Oxygen concentrations at the bottom of most of the Pacific north of 20°S are increased in the MC1 simulation compared with the PI simulation.

To summarise, changing from PI to MCO topography results in a warmer sea surface, causing a global reduction in oxygen solubility. Oxygen concentrations increase in the Pacific ocean north of 25 °S and below 1000 m depth, as a result of CAS through-flow at central latitudes and a reduction in biological activity in northern latitudes. Most of the Atlantic (with the exception of a small region bathed in AAIW, Figure 9a) is less oxygenated as a result of poorer ventilation in the deep ocean and increased biological activity in the upper ocean.

3.4.2 Oceanic Oxygen in the MC2 and MC3 experiments

We compare the MC2 and MC3 BGC simulations to that of MC1 to assess the impact of re-organised ocean circulation on biogeochemistry in much warmer simulations.

https://doi.org/10.5194/egusphere-2026-3378
Preprint. Discussion started: 1 July 2026

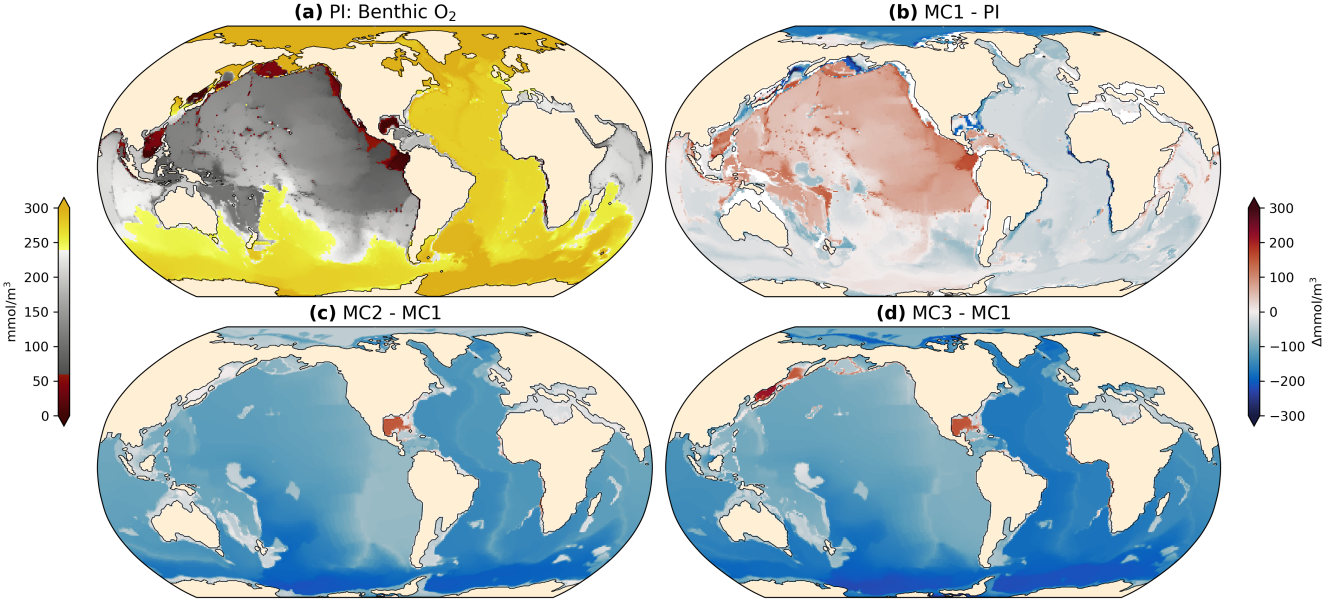

Figure 10. Oxygen concentration in mmol/m^3 for (a) PI and anomalies for (b) MC1 - PI, (c) MC2 - MC1 and (d) MC3 - MC1 at the bottom of the ocean (lowest wet grid cell in each column).

In both MC2 and MC3, O_2^{sat} decreases basin-wide in the Pacific and the Atlantic. The patterns of change are similar for MC2 and MC3 but the magnitude of change is larger in the MC3 simulation (Figures 8f, 8j, 9f, 9j) due to higher sea surface temperatures (Figure A1, A3).

In the MC3 simulation there is a reduction in AOU from $\sim$ 400 m to $\sim$ 2000 m in the tropical and subtropical Pacific and from $\sim$ 400 m to $\sim$ 3000 m in the north Pacific (Figure 8k). This anomaly is strongest at a depth of $\sim$ 1000 m in the north Pacific. Changes to AOU coincide with changes in water ventilation almost everywhere, however the negative (red) AOU anomaly extends deeper than the age anomaly (Figure 8k, 8l). This implies that depths greater than $\sim$ 1500 m reductions in AOU are attributable to reductions in export production rather than increased circulation. In the MC2 simulation the reductions in North Pacific age and AOU are weaker and have a smaller extent than in MC3 (Figure 8g, 8h).

Compared with MC1, MC2 and MC3 feature greater horizontally averaged detritus concentrations in the upper ocean (above $\sim$ 150 m depth) in both the Atlantic and Pacific basins (Figure 11a, 12a) and have increased detritus concentrations averaged above 60 m across almost the entire ocean. This includes areas with reduced export production between 200 and 300 m (compare first and second row of Figure A10). Averaged between 2000 and 3000 m, MC2 and MC3 have reduced detritus concentrations across the entire ocean, with strongest anomalies in the Southern Ocean and the tropical Pacific (Figure A10 bottom row). Below 3000 m detrital nitrogen concentrations in the Atlantic and the Pacific of MC2 and MC3 are near zero (Figure 11a, 12a). This shift occurs as the MC2 and MC3 simulations are globally hotter than MC1 throughout the water column causing more rapid remineralisation of detritus in the upper ocean, and allowing very little detritus to reach the deep ocean.

https://doi.org/10.5194/egusphere-2026-3378
Preprint. Discussion started: 1 July 2026

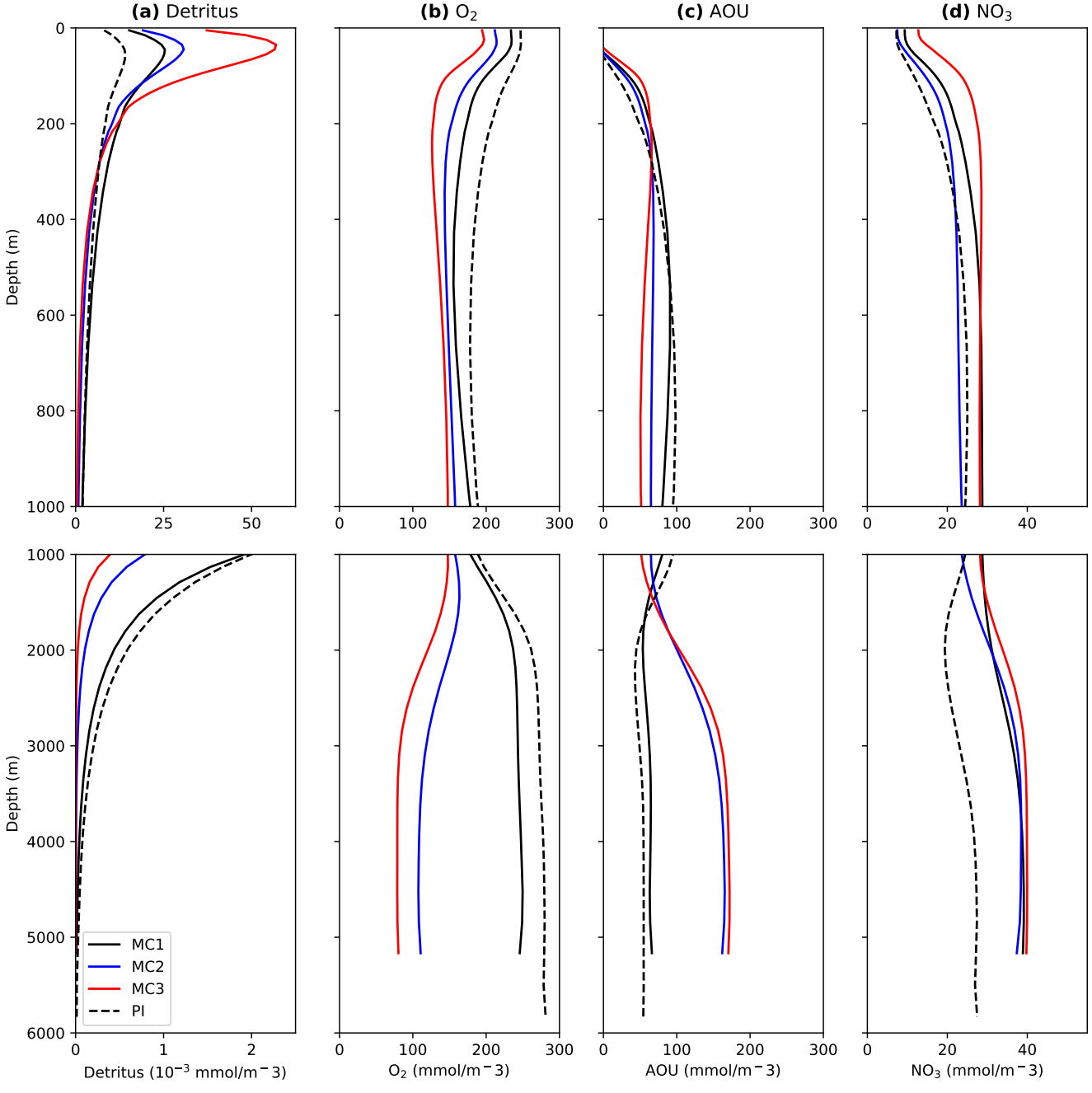

Figure 11. Atlantic Ocean horizontally averaged (a) detritus concentrations (10^{-3} mmol/m^3 of nitrogen), (b) oxygen concentration (mmol/m^3), (c) apparent oxygen utilisation (mmol/m^3) and (d) NO_3 (mmol/m^3). Note that the vertical and detritus concentration scales change between the upper and lower panels.

https://doi.org/10.5194/egusphere-2026-3378
Preprint. Discussion started: 1 July 2026

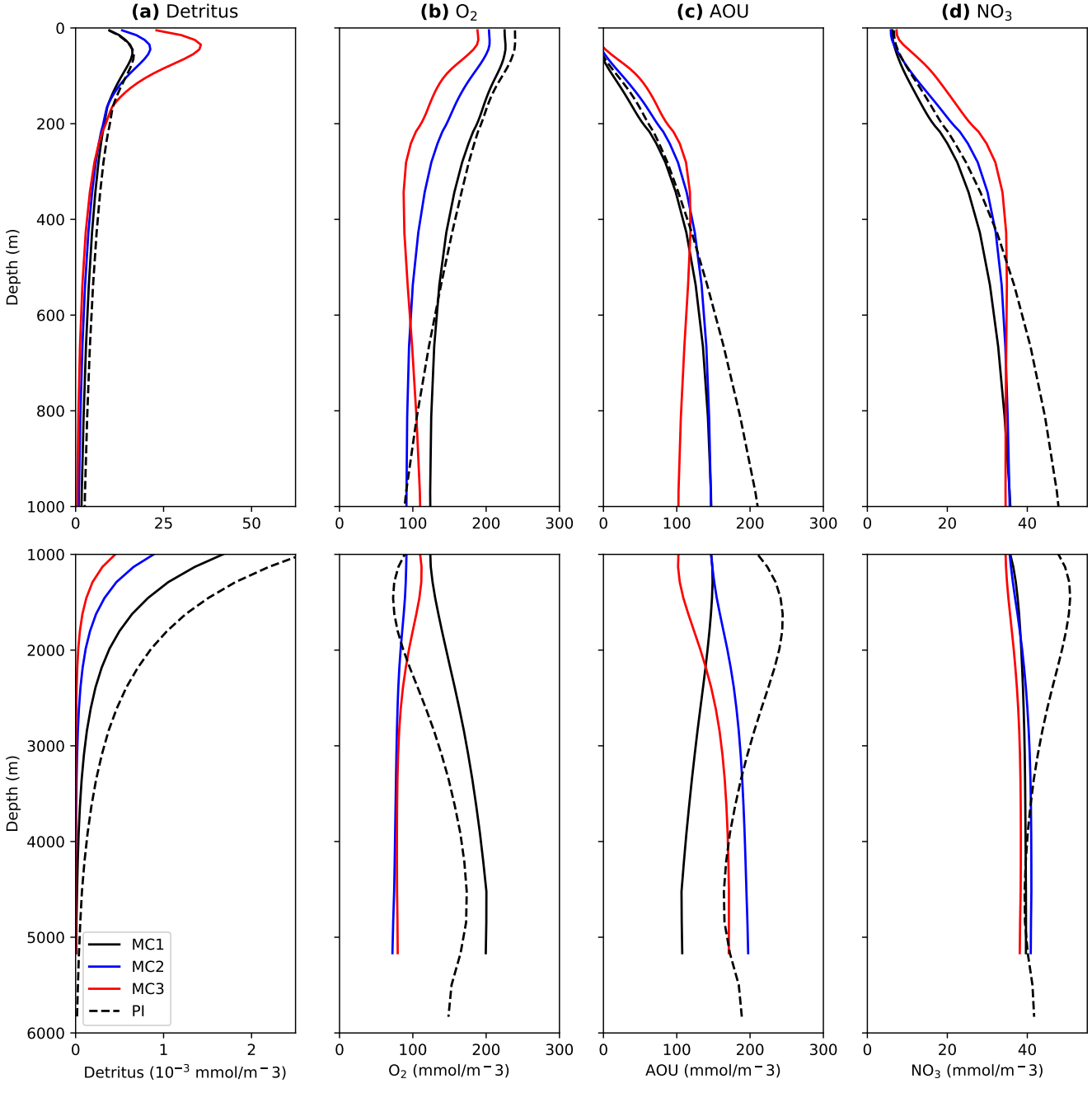

Figure 12. Pacific Ocean horizontally averaged (a) detritus concentrations (10^{-3} mmol/m^3 of nitrogen), (b) oxygen concentration (mmol/m^3), (c) apparent oxygen utilisation (mmol/m^3) and (d) NO_3 (mmol/m^3). Note that the vertical and detritus concentration scales change between the upper and lower panels.

https://doi.org/10.5194/egusphere-2026-3378
Preprint. Discussion started: 1 July 2026

In the Atlantic both MC2 and MC3 are well ventilated above $\sim$ 1500 m as a result of vigorous intermediate water formation (Section 3.3, Figure 9). In addition to better ventilation there is a reduction in export production over most of the tropical and subtropical Atlantic for both MC3 and MC2 (Figure A10e,f). The combination of reduced export production and increased ventilation results in greater oxygenation above 1500 m in the tropical Atlantic in the elevated pCO_2 simulations compared to MC1.

Weaker NADW and a lack of AABW formation result in increased AOU below 2000 m with a maximum at $\sim$ 4000 m depth in the Atlantic ocean (Figure 11c). Owing to better NPIW formation in the elevated CO_2 simulations, in MC2 and MC3 AOU averaged across the Pacific decreases with depth between $\sim$ 300 m and $\sim$ 1000 m and increases with depth below $\sim$ 1000 m owing to the lack of AABW formation in these simulations (Section 3.3) which results in a poorly ventilated Pacific seafloor (Figure A6).

The MC2 and MC3 simulations have reduced bottom oxygen concentrations across almost the entire seafloor (Figure 10). However, there are positive anomalies at deep water formation sites in the Gulf of Mexico in MC2 and MC3 and the North West Pacific in MC3 (Figure 10).

3.4.3 Extent of hypoxia and anoxia

Simulation	PI	MC1	MC2	MC3
Oxygen-rich	0.33	0.19	0.005	0.0012
Hypoxic	0.15	0.034	0.13	0.050
Anoxic	0.031	0.0047	0.0042	0.0037

Table 3. Fraction of whole ocean volume that is oxygen-rich ($\geq$ 240 mmol/m^3), hypoxic ($\leq$ 62 mmol)/m^3) and anoxic ($\leq$ 10 mmol)/m^3) for the PI control simulation, MC1, MC2 and MC3.

Of the four simulations analysed in this study, the PI simulation has the highest volume of anoxic, hypoxic and oxygen-rich waters (Table 3) having stronger ventilation of oxygen saturated waters in polar regions (Figures 13, 14) and much larger and more intense oxygen deficient zones (ODZs) in the Pacific than the MC1 simulation (Figure 13). Compared with MC1, the MC2 simulation shows a large increase in the volume of hypoxic waters, a large decrease in the volume of oxygen-rich water and a small decrease in anoxic water volume. The decrease in oxygen-rich water fraction is a result of the decrease in bottom and deep water formation in both the Pacific and the Atlantic (Figures 13, 14). The increase in hypoxic waters is mostly attributable to the North Pacific (Figure 13), where poorer ventilation in some areas and the basin-wide reduction in solubility results in broadly decreasing oxygen concentrations (Figure 8). The MC3 simulation has the lowest fraction of oxygen-rich and anoxic waters of any of the simulations analysed in this study; only the MC1 simulation has slightly less hypoxic waters (Table 3). The reduction in saturated water fraction, similar to the MC2 simulation, is the result of reduced oxygen solubility and sluggish circulation. The slight increase in hypoxia compared with the MC1 simulation can mostly be attributed to the expansion of the ODZ in the tropical Pacific, while other regions that are hypoxic in MC1 and MC2 are better oxygenated

https://doi.org/10.5194/egusphere-2026-3378
Preprint. Discussion started: 1 July 2026

in MC3. Despite being poorly ventilated, the MC3 simulation has very little anoxic waters, and despite lacking bottom water formation MC3 does not display benthic anoxia.

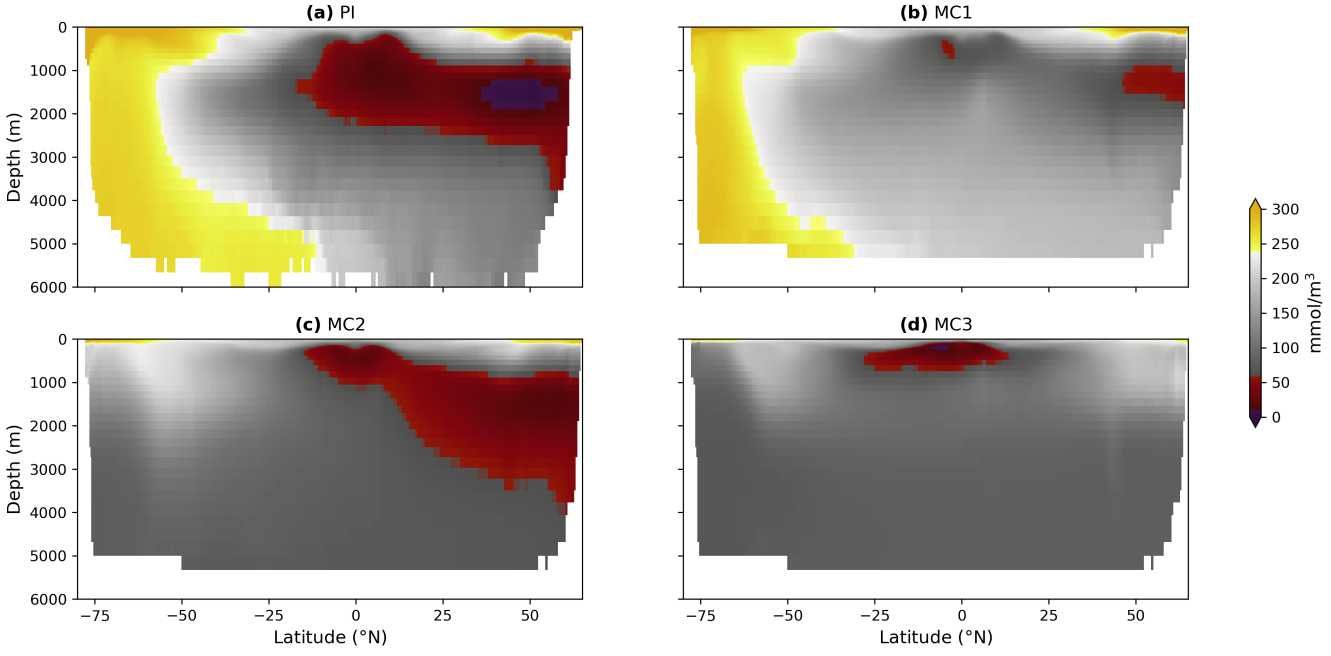

Figure 13. Zonally averaged oxygen concentrations in the Pacific basin in mmol/m^3 for a) the PI control run, b) MC1, c) MC2 and d) MC3. Areas with average concentrations between 62 and 10 mmol/m^3 are coloured red and areas with concentrations below 10 mmol/m^3 are coloured purple to indicate hypoxia and anoxia. Regions with oxygen concentrations above 240 mmol/m^3 are shown in yellow.

Other than for the North Pacific ocean in MC2, MC2 and MC3 feature basin wide low, but not hypoxic oxygen concentrations below 2000 m (Figure 13c, 13d, 14c, 14d). MC2 and MC3 lack well-oxygenated bottom and deep waters, which are present in MC1 and the PI simulation (Figure 14). On the ocean floor, the elevated pCO_2 simulations do not feature large areas of hypoxia or anoxia but do display negative oxygen anomalies compared with MC1 (Figure 10 bottom row).

4 Discussion

There are few examples of CMIP6-class ESMs that have run long ($>$ 1 kyr) simulations that lack bottom water formation (Zhu et al., 2019). Running such a scenario has enabled us to investigate ocean biogeochemistry with a relatively high resolution model. Our stratified simulations and use of an acceleration method enable us to investigate equilibrated biogeochemistry in a stratified state under boundary conditions similar to the Earth's warm future. Overall, our results suggest that while stagnant circulation patterns do create global reductions in dissolved oxygen, they are not sufficient to generate a large-scale OAE within the framework of our model, because of the temperature-driven shoaling of remineralisation depth.

https://doi.org/10.5194/egusphere-2026-3378
Preprint. Discussion started: 1 July 2026

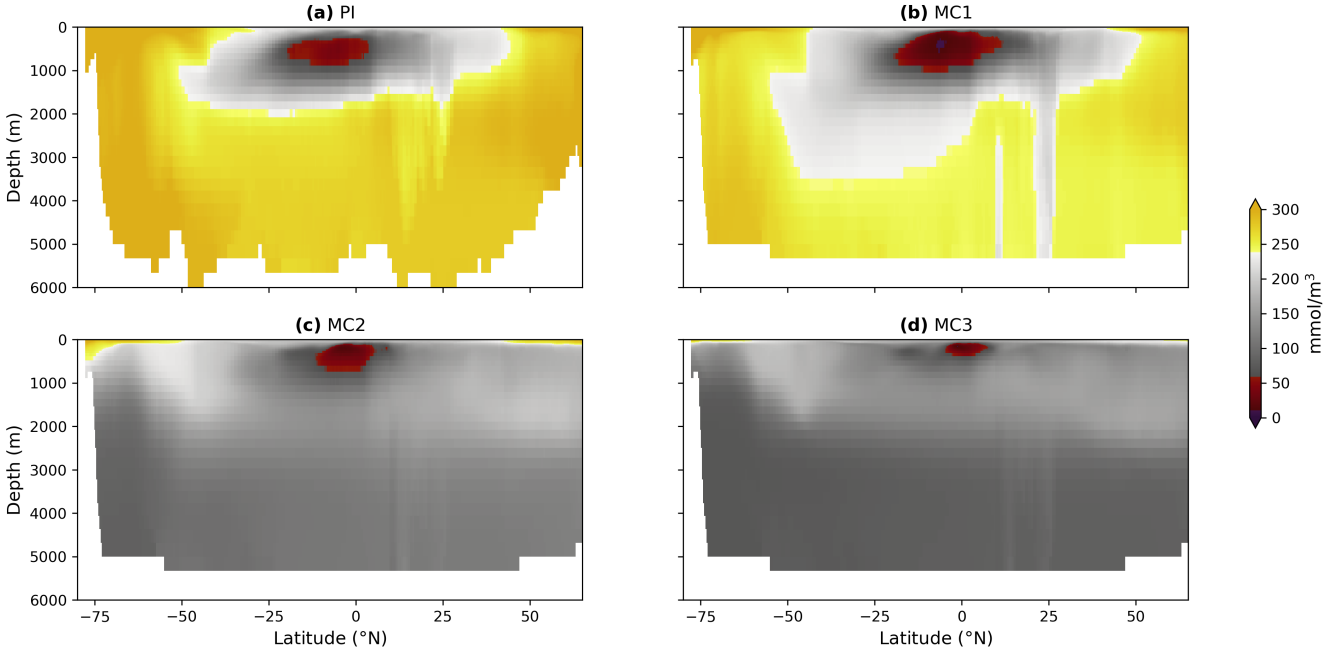

Figure 14. Zonally averaged oxygen concentrations in the Atlantic basin in mmol/m^3 for a) the PI control run, b) MC1, c) MC2 and d) MC3. Areas with average concentrations between 62 and 10 mmol/m^3 are coloured red and areas with concentrations below 10 mmol/m^3 are coloured purple to indicate hypoxia and anoxia. Regions with oxygen concentrations above 240 mmol/m^3 are shown in yellow.

4.1 Representation of the MCO

Our elevated pCO_2 simulations do not capture the flattening of the meridional temperature gradient as indicated by proxies for the MCO, a problem shared with other Miocene modelling efforts (e.g. Burls et al., 2021). Our work adds to a body of evidence that ESMs struggle to represent climates outside what they have been tuned for (Burls and Sagoo, 2022). The unventilated ocean state, caused by a cold start initialisation in our spin-up, is also most likely not representative of an MCO equilibrium climate, for which we had initially intended to simulate biogeochemistry. This possibly transient state is caused by rapid warming of the upper ocean, whereas a fully-equilibrated Miocene deep ocean may have better ventilation. Our simulations might, however, be representative of a transient behaviour of the ocean when forced with rapidly increasing greenhouse gas concentrations. Work investigating the effect of rapid ice sheet meltwater forcing has projected an analogous shutdown in AABW formation in future high emissions scenarios (Lago and England, 2019). Furthermore, there are some similarities between the circulation in our elevated pCO_2 experiments and in future high emissions scenario experiments using ACCESS-ESM1.5 (Figure A11).

https://doi.org/10.5194/egusphere-2026-3378
Preprint. Discussion started: 1 July 2026

4.2 Shift in remineralisation depth

In WOMBAT, remineralisation rate R is dependent on detritus concentrations and an exponential of temperature and is represented as:

$$R = \mu_d D$$

where:

$$\mu_d = 0.048\, b^{cT}\,\text{day}^{-1} \quad \text{above 180 m}$$

and

$$\mu_d = 0.024\, b^{cT}\,\text{day}^{-1} \quad \text{below 180 m}$$

where D is detritus concentration in mmol/m^3 and, $c = 1.0\,^{\circ}\text{C}^{-1}$, $b = 1.066$ and T is Temperature in °C (Oke et al., 2013; Ziehn et al., 2020). This parametrisation was optimised for the Southern Ocean under modern conditions (Law et al., 2017). All of our MCO experiments, particularly the elevated CO_2 simulations, are warmer then the conditions for which WOMBAT was optimised.

Biological activity at the surface is generally enhanced in the MC2 and MC3 simulations, resulting in higher detritus concentrations in the upper 100 m of the ocean. Increased temperatures in these simulations cause detritus to rapidly remineralise near the surface, reducing export production and transport of nutrients out of the photic zone (Kvale et al., 2015).

Being a component of a computationally efficient ESM, WOMBAT is necessarily a lightweight marine BGC model that does not feature ecological details which may be impact the representation of anoxia at depth. For example, WOMBAT only has 1 phytoplankton and detritus type to model primary productivity and nutrient transport (Oke et al., 2013), but the ecological balance between different species of phytoplankton in primary production may be critical to benthic detritus transport and deoxygenation in stratified oceans (Kemp and Villareal, 2013; Mancini et al., 2024). Further, WOMBAT's detritus sinking and remineralisation dynamics are simplistic. Detritus sinks at a constant rate of 24 m per day. The parametrisation of remineralisation (which is solely dependent on temperature) was optimised for modern ocean temperatures and is almost certainly inadequate for our elevated pCO_2 simulations. Use of a BGC model with more detailed sinking dynamics (e.g Buchanan et al., 2025) and with a more complex representation of primary production and bacterial respiration (e.g. Buchanan et al., 2026) would result in significantly different transport of detritus to the ocean floor. Our MC2 and MC3 simulations maintain a delicate balance between near zero detritus transport and near zero oxygen transport for over 1000 years in the deep ocean. Any transport of detritus, even if it is weak and intermittent, would alter the oxygen profile of the deep ocean.

4.3 Representation of OAE formation

Our MC2 and MC3 simulations are investigations of the preservation hypothesis of OAE formation with npCO_2 and topography that are more similar to modern or futures conditions than periods associated with OAEs in the proxy record. The physical stability of MC2 and MC3 ocean states is difficult to assess without long, expensive and computationally unfeasible integration times. Given that the deep ocean continues to gain heat in both simulations, and that MC2 begins to show increasing circulation

https://doi.org/10.5194/egusphere-2026-3378
Preprint. Discussion started: 1 July 2026

towards the end of its integration, the stratified states represented in our simulations are likely unstable. Below 3000 m detritus concentrations are near zero in the MC2 and MC3 simulations, demonstrating a limitation in the preservation hypothesis of OAE formation, especially in the deep ocean, within the framework of our BGC model.

Given that our simulations are essentially as unventilated as possible in the deep ocean, to achieve ocean anoxia under the preservation hypothesis alone would either require similar stratification at lower temperatures, as this would allow more detritus to reach the deep ocean before being remineralised, or a different temperature-related behaviour of remineralising bacteria. However, in proxy records, OAEs are always associated with elevated pCO_2 and temperature (Rampino et al., 2023). Simulations of OAEs using models of lower resolution than ACCESS-ESM1.5 have suggested that increased nutrient runoff into the ocean is essential to triggering an OAE with bathymetry boundary conditions very different to ours, such as the Devonian (420-370 Ma, Gérard et al. (2025)) and Mid Cretaceous, ($\sim$ 94 Ma, Cui et al. (2025)), and this could be a significant factor under our boundary conditions as well. Increased nutrient runoff may still fail to overcome the rapid remineralisation of detritus in the upper ocean and fail to yield widespread benthic anoxia; possibly only producing anoxia in shallower parts of the ocean, associated with nutrient run off or upwelling. Our simulations failure to produce anoxia despite near-zero benthic oxygen transport highlights the need for a better understanding and a better representation of detritus sinking and remineralisation in BGC models.

4.4 Limits of Anderson acceleration

A limitation of AA in its current form (Khatiwala, 2023) is that it must be applied to dynamically passive tracers, since it requires an identically repeating physical circulation to achieve the acceleration. This complicates spin up strategy and necessitates a trade off between equilibrating biogeochemistry for a "frozen" circulation regime or allowing it to evolve in tandem with the physical simulation. It has been suggested that AA could also be extended to dynamic tracers such as temperature and salinity, by using iterative passive tracers (Khatiwala, 2024), creating a "passive temperature" and "passive salinity" tracer, that can be accelerated towards equilibrium using a given (repeating) physical circulation. After a suitable interval (e.g. 50 years), the accelerated passive tracers could then be used to re-initialise the dynamic temperature and salinity, with alternation between active (online) and passive (AA) spinup stages. Preliminary investigation of this method with ACCESS-ESM1.5 found that this was not feasible with the current code base, since a different surface flux regime would be needed than is currently available. But if a scheme of alternating passive and active spin-up could be implemented, this could provide major benefits in accelerating the dynamic spinup of temperature and salinity in a fully-coupled earth system model.

5 Conclusions

We used a novel method to generate well equilibrated marine biogeochemistry for 3 paleoclimate simulations. The BGC simulations produced by our Anderson-accelerated spinup have very low remaining drift in oxygen concentrations. This work thus demonstrates how acceleration methods such as Anderson Acceleration enable efficient equilibration of oceanic biogeochemistry for an ESM. Our testing of AA in ACCESS-ESM1.5 prior to this work produced an acceleration factor of 5-8 for ocean

https://doi.org/10.5194/egusphere-2026-3378
Preprint. Discussion started: 1 July 2026

oxygen. Although AA affects individual water masses differently, making defining an overall acceleration factor difficult, our biogeochemical spin up is likely equivalent to $\sim$ 5000 years including the long post AA integration.

The dual requirement for complex biogeochemical models and long integrations called for by our results motivates continued work on acceleration techniques for biogeochemical models of greater complexity than WOMBAT in future ESMs. The use of AA here is one of the first practical applications of acceleration methods in Earth system modelling. More effective ways to harness these methods are almost certainly possible.

Our simulations are not in physical equilibrium and therefore may be different to an MCO scenario with steady-state deep ocean temperatures. Instead, our work provides insight into potential ocean anoxia onset and changes to ocean circulation under rapid changes in climate, which is arguably more relevant to Earth's near future than an equilibrated MCO simulation. Our simulations were initialised from experiments using the same boundary conditions with the GFDL CM2.1 model, however they produce a different physical state. Recent work examining circulation in Miocene modelling efforts has found great variability in representations of circulation (Naik et al., 2025), and our results further suggest that models are able to produce many different representations of dynamics for boundary conditions different to those the models have been developed and tuned for.

The highly stratified ocean states in our simulations provided an opportunity to test ocean anoxia onset under the preservation hypothesis with a relatively high resolution ESM. We find that the combination of a hot ocean with high remineralisation rates and high levels of stratification produces a delicate equilibrium between near zero export production and near zero oxygen supply to the deep ocean. Our stratified simulations showed low benthic oxygen concentrations but no benthic anoxia. It is plausible that oxygen could be pushed towards anoxia with a more complex representation of biogeochemistry, particularly the representation of detritus sinking and remineralisation. Even so, our results suggest that when deep ocean ventilation shuts down, anoxia onset might not occur, or would at the very least be delayed. Although not tested explicitly by our work, our simulations support the findings of other simulations, which have suggested that increased nutrient content in the ocean is essential to triggering an OAE (Gérard et al., 2025; Cui et al., 2025), as we are unable to produce anoxia without enhanced nutrient runoff. Our work further suggests that the existence of large shallow seas would make widespread benthic anoxia more likely as they would be less affected by the shoaling of remineralisation depth.

The dramatic changes in circulation seen in our elevated $p\mathrm{CO}_2$ simulations bear some resemblance to changes that occur in high emissions experiments using the same ESM. As evidenced by our work and the work of other modelling groups, there is great variability in the representation of ocean circulation under changed boundary conditions, and therefore still great uncertainty in the long term future of ocean circulation and impacts to ocean ecosystems, in a mid-high emissions future.

Code and data availability. The PI data is taken from simulation "PI-02" (Mackallah et al., 2022), and used as a baseline comparison to the MCO simulations. SSP5-85 data was taken from CMIP6 run r8i1p1f1. Both were used in their non CMORised format. Averages and time series used to produce the plots presented here are available at https://doi.org/10.5281/zenodo.20618892 and the code used is available at https://github.com/benjWA/MCO$_O AE_p aper$

https://doi.org/10.5194/egusphere-2026-3378
Preprint. Discussion started: 1 July 2026

Appendix A

A1 Anderson Acceleration

Once model physics are restricted to a repeating cycle, direct integration of biogeochemistry can be represented by taking a vector $\boldsymbol{x}_k$ which represents the current state of the simulation (the values for all tracers in all grid cells) and applying a time evolution function to that vector to produce a new vector, until the new vector and the previous vector are the same, representing convergence (Khatiwala, 2023). Given an initial condition $\boldsymbol{x}_0$ and a time evolution function $\boldsymbol{g}$ (i.e. the model and it's boundary conditions) this can be represented as:

$$\boldsymbol{x}_{k+1} = \boldsymbol{g}(\boldsymbol{x}_k)$$

where $k = 0, 1, ...$ until convergence:

$$\boldsymbol{g}(\boldsymbol{x}_k) = \boldsymbol{x}_k$$

This can be equivalently defined using a residual function $\boldsymbol{f}$:

$$\boldsymbol{f}(\boldsymbol{x}_k) = \boldsymbol{g}(\boldsymbol{x}_k) - \boldsymbol{x}_k$$

so the problem becomes solving for:

$$\boldsymbol{f}(\boldsymbol{x}_k) = \boldsymbol{0}$$

In practice, models do not achieve strict mathematical convergence. Instead models are spun up until they achieve a state of quasi equilibrium, meaning there is little year on year change (Yool et al. (2020)). Instead of continuously reapplying the same function over and over, AA uses a number (m_k) of previous states ($\boldsymbol{x}_{k-m_k}$, $\boldsymbol{x}_{k-m_k+1}$ ... $\boldsymbol{x}_{k-1}$) in addition to the most recent state ($\boldsymbol{x}_k$) and takes a weighted average of them (Khatiwala, 2023):

$$\boldsymbol{x}_{k+1} = \sum_{j=0}^{m_k} \alpha_j^{(k)} \boldsymbol{g}(\boldsymbol{x}_{k-m_k+j})$$

where m_k is the maximum number of previous iterations included. Iteration weights α are chosen by solving the least squares problem:

$$\text{minimize} \left\| \sum_{j=0}^{m_k} \alpha_j^{(k)} \boldsymbol{f}(\boldsymbol{x}_{k-m_k+j}) \right\|_2^2$$

Weights α are subject to the normalisation:

$$\sum_{j=0}^{m_k} \alpha_j^{(k)} = 1$$

If the number of previous iterates is less than m_k then all previous iterates are used. For this reason the algorithm does not take full advantage of past states until step m_{k+1}. Setting $m_k = 0$ (that is, to only use the current iteration) reproduces DI with a fixed physical system. The $\boldsymbol{g}$ function only depends on the biogeochemistry vector since AA uses a repeating physical cycle.

https://doi.org/10.5194/egusphere-2026-3378
Preprint. Discussion started: 1 July 2026

Compared with the climate model used in this project, the AA algorithm has very little computational demand (Khatiwala, 2023). AA treats the $\boldsymbol{g}$ function as a "black box", meaning it does not need to interact with the model other than receiving an input from the model $\boldsymbol{g}(\boldsymbol{x}_k)$, without any knowledge to how the model functions. This makes AA a versatile method that can be applied to any biogeochemical model that uses iterative time steps.

A2 Implementation of Anderson Acceleration in ACCESS-ESM1.5

Our AA implementation is based on that of Khatiwala (2023). A Matlab version of the AA algorithm is provided from that implementation. This implementation requires a model specific $\boldsymbol{g}$ function and a driver script supplied by the user. These take the form of two Matlab scripts which may be found at this project's GitHub repository (Anthonisz, 2025).

In this implementation the minimum time for a cycle k is one year. Although in principle k could be as short as one time step within the model it must be at least one year to capture a seasonal cycle. The number of years per cycle k can be changed by modifying the $\boldsymbol{g}$ function and associated driver script. If the cycle length is only 1 year then temporary modes such as El Niño events, or intermittent circulation variability (e.g Figure A7) have the potential to bias simulation evolution over long term trends. Increasing the cycle length beyond 1 year can therefore prevent biasing as a result of interannual variability within the physical circulation, but reduces the computational savings of the algorithm. Increasing iteration length also increases the "warm up" period, since acceleration relies on accumulating many steps of the algorithm. The ideal cycle length depends on which behaviours are of greatest interest and may vary between simulations. We used a cycle length of 10 years as a compromise between accounting for interannual variability and leveraging the acceleration algorithm.

The number of previous iterations stored (m_k) can be modified. We set $m_k = 10$ for the MCO simulations. In its default configuration, once one cycle k is completed, the $\boldsymbol{g}$ function deletes the saved intermediate states produced during the cycle and the simulation is restarted from the same physical initial conditions but with a new biogeochemical profile provided by AA. This means that only the oceanic biogeochemistry is evolving. This method was chosen as work using a similar method showed that no acceleration would occur unless the physical circulation was kept in an identically repeating pattern for each iteration (Pasquier et al., 2025). Since biogeochemical evolution is strongly dependent on the physical simulation, it is ideal if the physics of the simulation are well equilibrated before spinning up with AA.

https://doi.org/10.5194/egusphere-2026-3378
Preprint. Discussion started: 1 July 2026

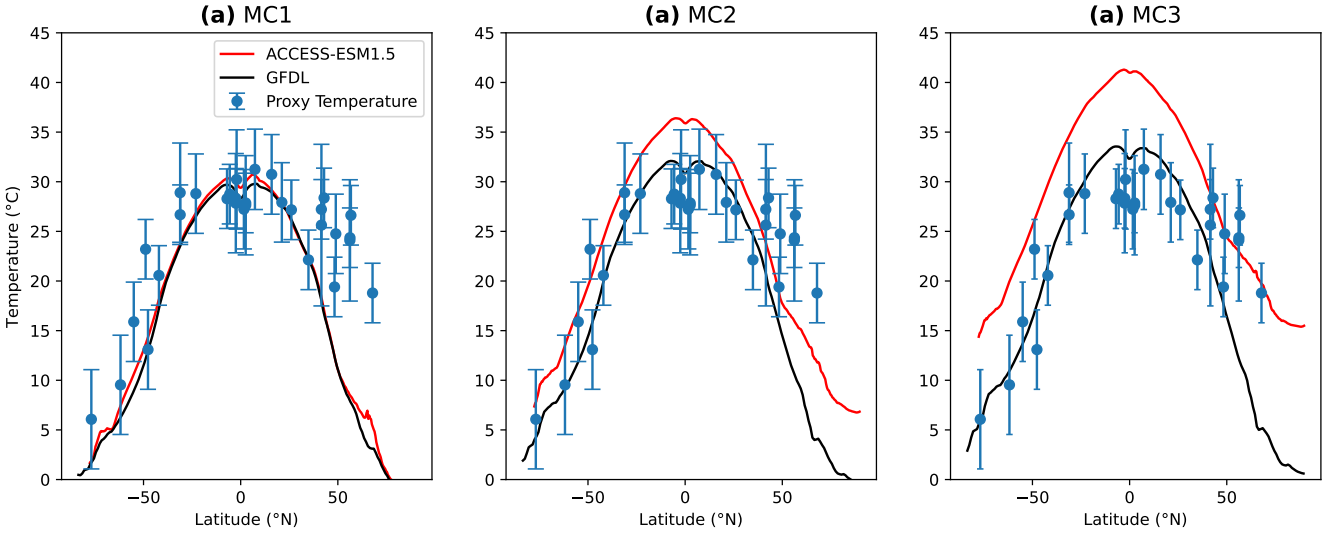

Figure A1. Zonal mean sea surface temperature (°C) for the ACCESS-ESM1.5 MCO simulations (red line) compared with the GFDL simulations from which they were initialised (black line). Proxy estimates (blue dots) are from Burls et al. (2021).

https://doi.org/10.5194/egusphere-2026-3378
Preprint. Discussion started: 1 July 2026

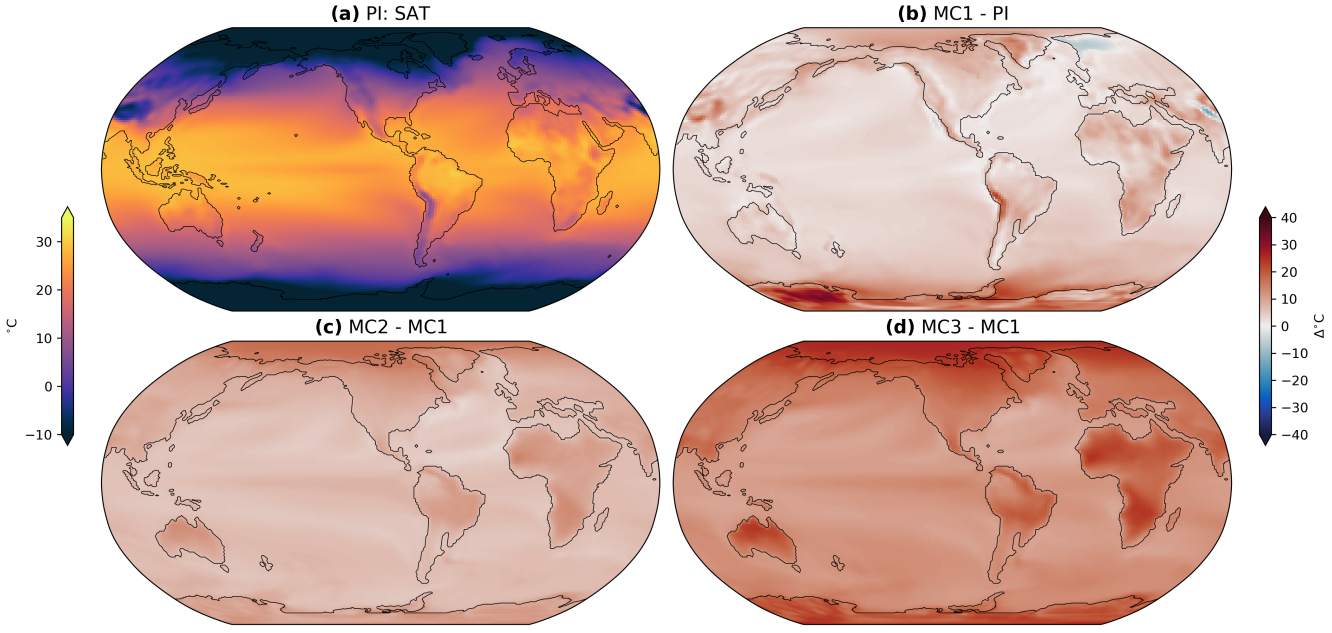

Figure A2. Near Surface (1.5 m) Air Temperature (SAT, °C) for the PI control (a), anomaly between MC1 and PI (b), anomaly between MC2 and MC1 (c) and anomaly between MC3 and MC1 (d).

https://doi.org/10.5194/egusphere-2026-3378
Preprint. Discussion started: 1 July 2026

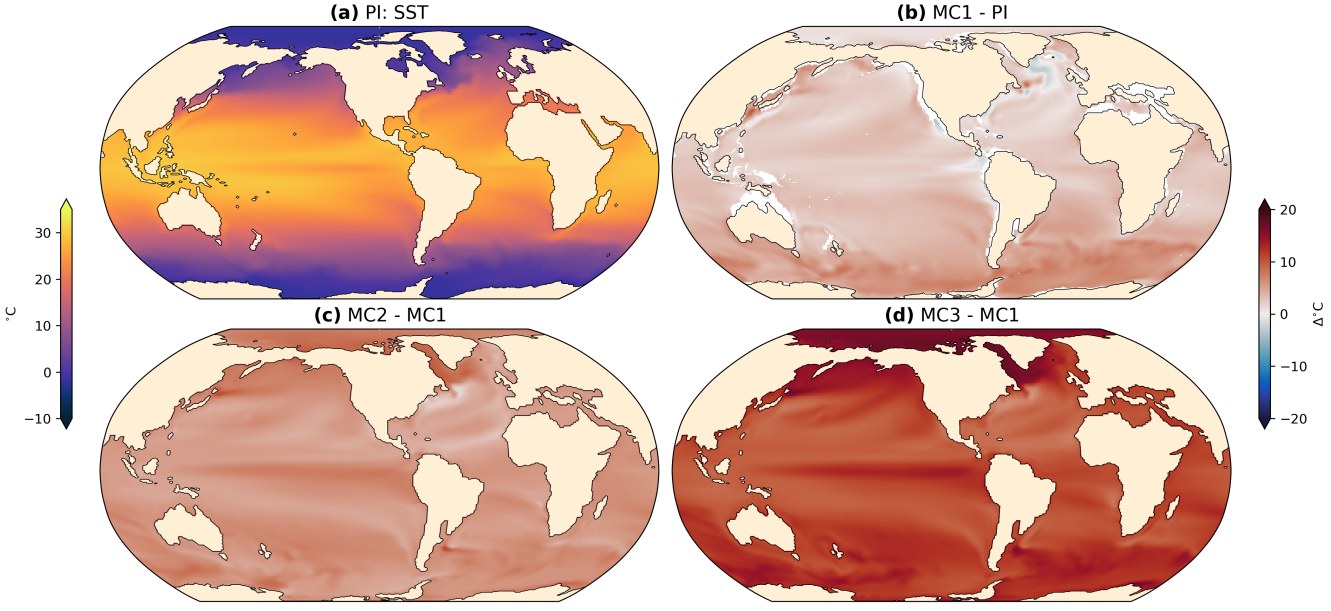

Figure A3. Sea Surface Temperature (SST, °C) for the PI control (a), anomaly between MC1 and PI (b), anomaly between MC2 and MC1 (c) and anomaly between MC3 and MC1 (d).

https://doi.org/10.5194/egusphere-2026-3378
Preprint. Discussion started: 1 July 2026

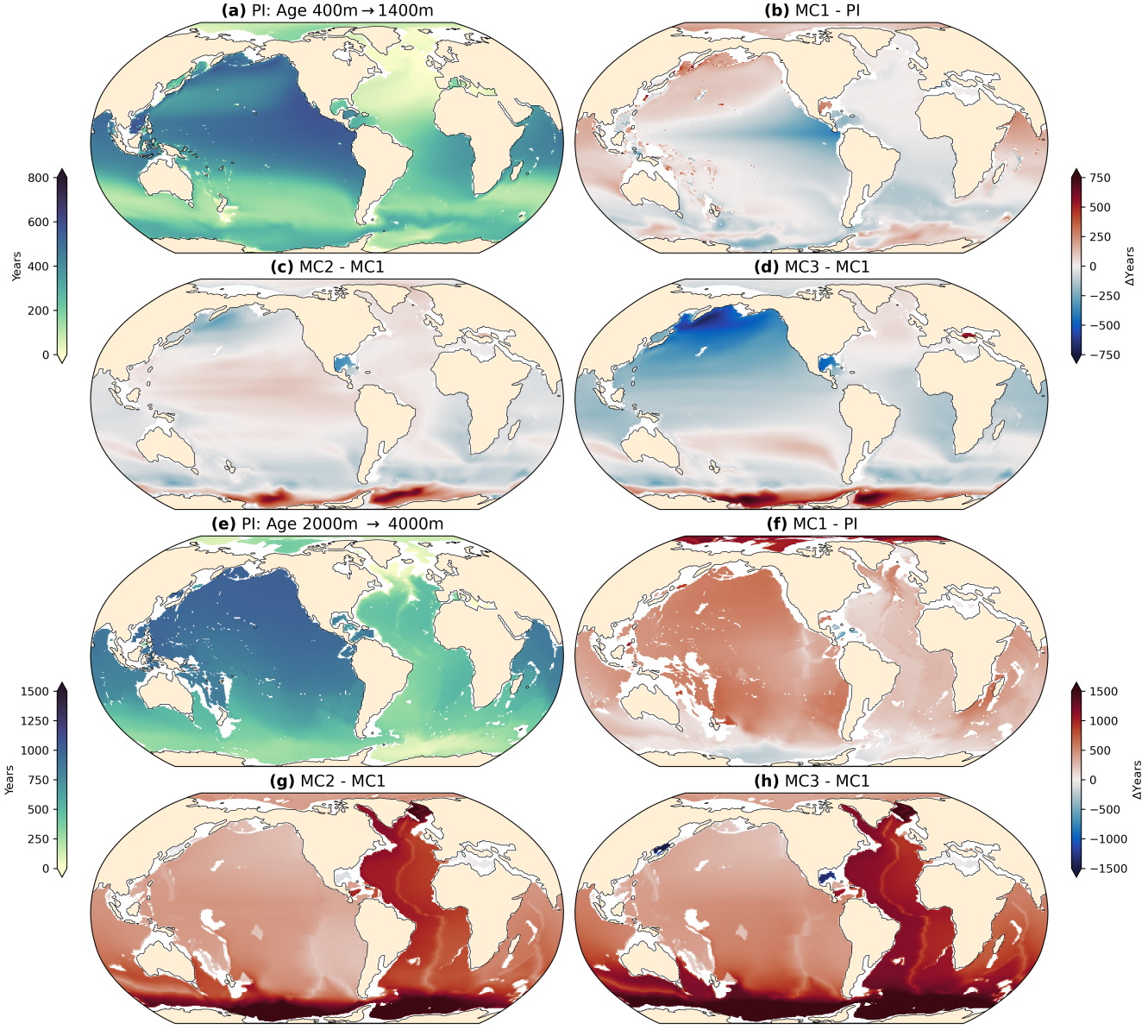

Figure A4. Water age averaged between 400 and 1400 m for PI (a), and anomalies for the same depth range for MC1 - PI (b), MC2 - MC1 (c), and MC3 - MC1 (d). Water age averaged between 2000 and 4000 m for PI (e), and anomalies for the same depth range for MC1 - PI (f), MC2 - MC1 (g), and MC3 - MC1 (h). Note that colour scale is changed between subplots a-d and e-h for clarity.

https://doi.org/10.5194/egusphere-2026-3378
Preprint. Discussion started: 1 July 2026

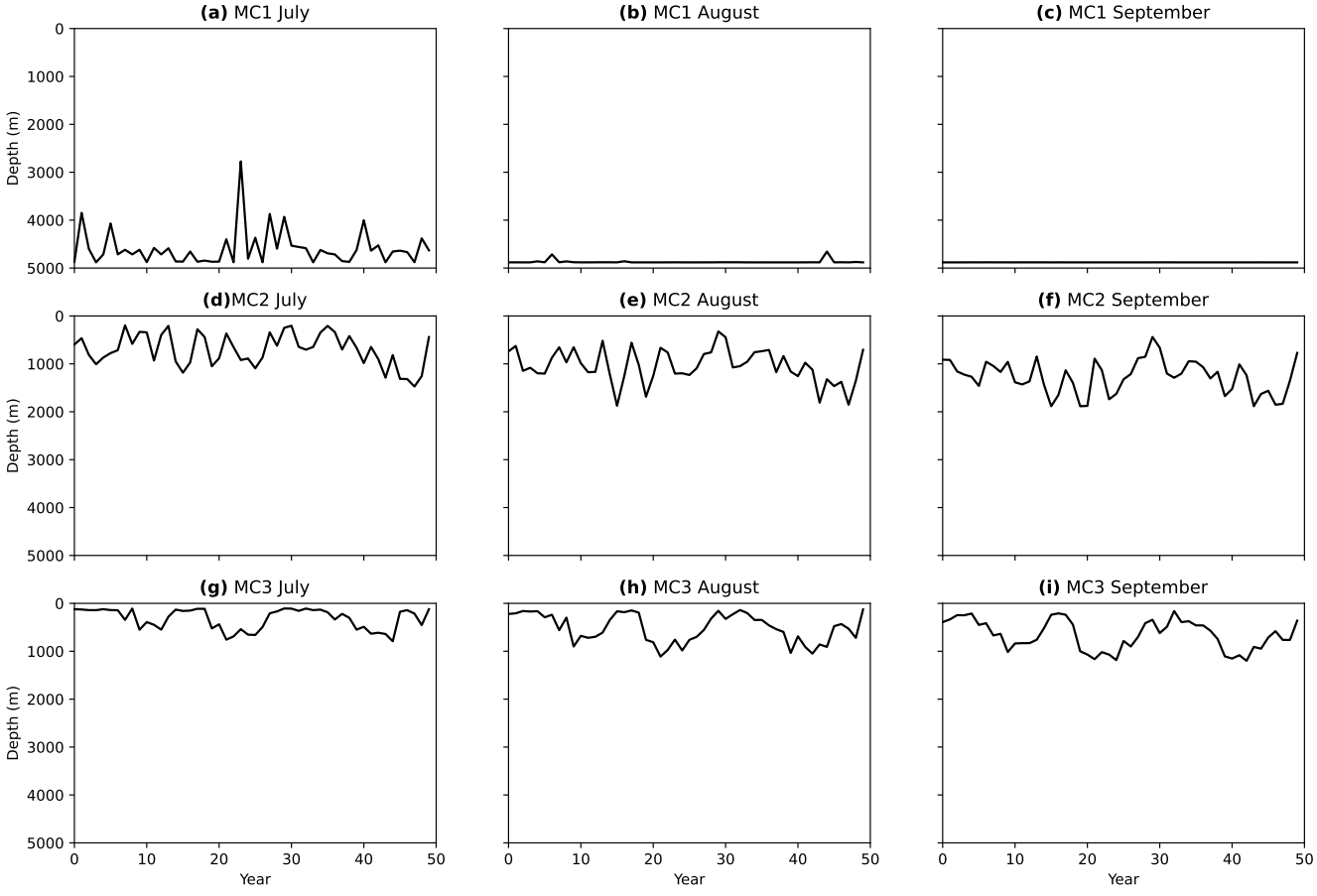

Figure A5. Timeseries of the maximum monthly average mixed layer depth in the Ross and Weddell Seas for the 50 year analysis period in July (left column), August (middle column) and September (right column) for MC1 (top row), MC2 (middle row) and MC3 (bottom row) simulations.

https://doi.org/10.5194/egusphere-2026-3378
Preprint. Discussion started: 1 July 2026

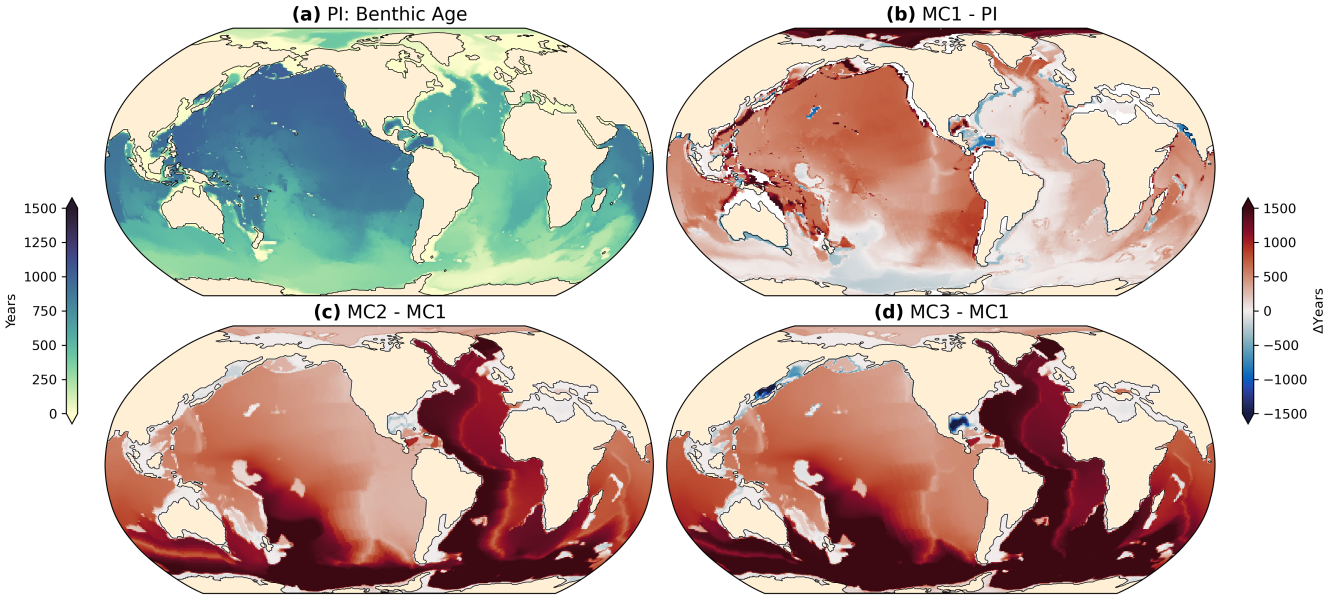

Figure A6. Water age at the bottom of the ocean (lowest wet grid cell) for PI (a) and anomalies between MC1 and PI (b), MC2 and MC1 (c) and MC3 and MC1 (d)

https://doi.org/10.5194/egusphere-2026-3378
Preprint. Discussion started: 1 July 2026

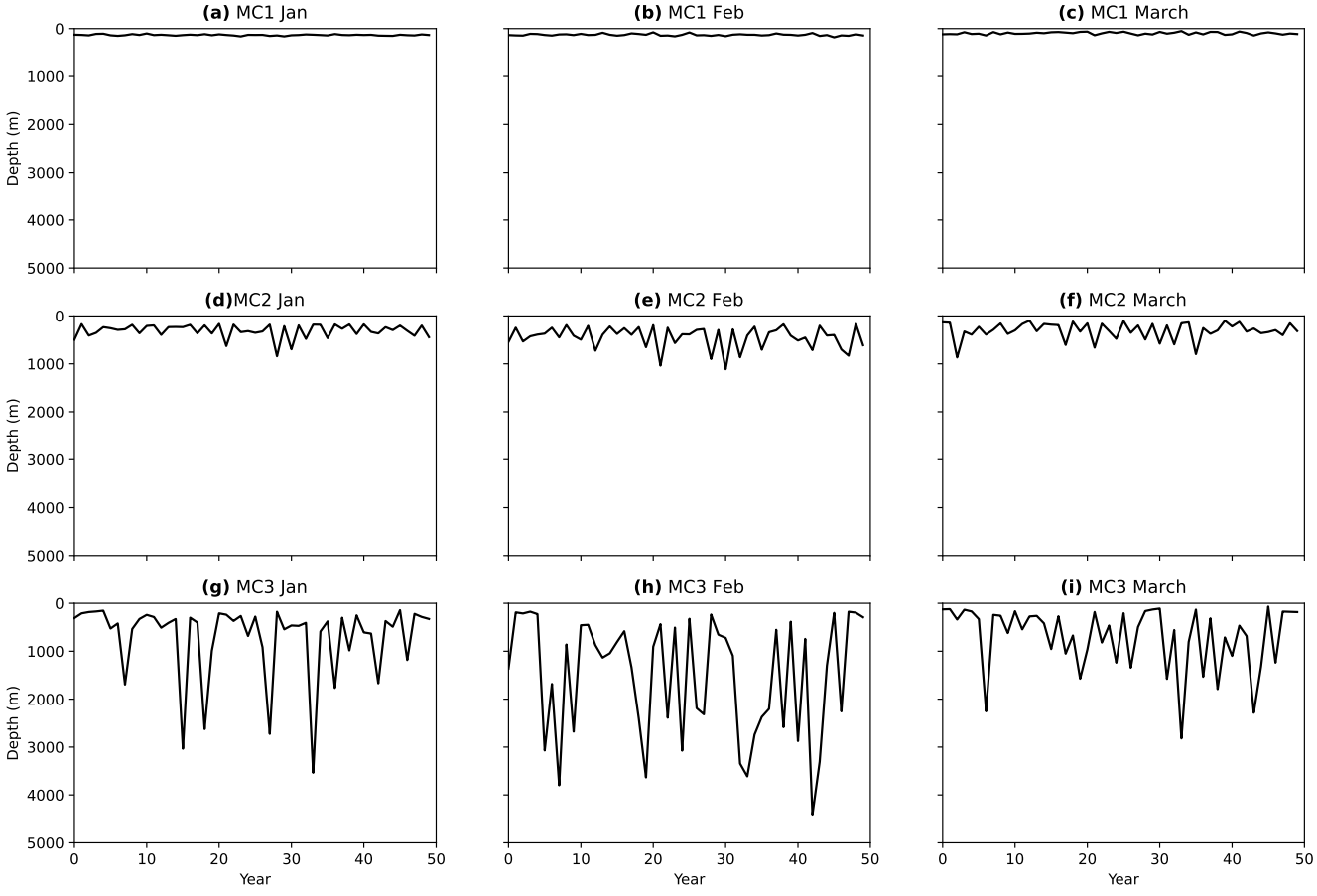

Figure A7. Timeseries of the maximum monthly average mixed layer depth in the Gulf of Mexico for the 50 year analysis period in January (left column), February (middle column) and March (right column) for MC1 (top row), MC2 (middle row) and MC3 (bottom row) simulations.

https://doi.org/10.5194/egusphere-2026-3378
Preprint. Discussion started: 1 July 2026

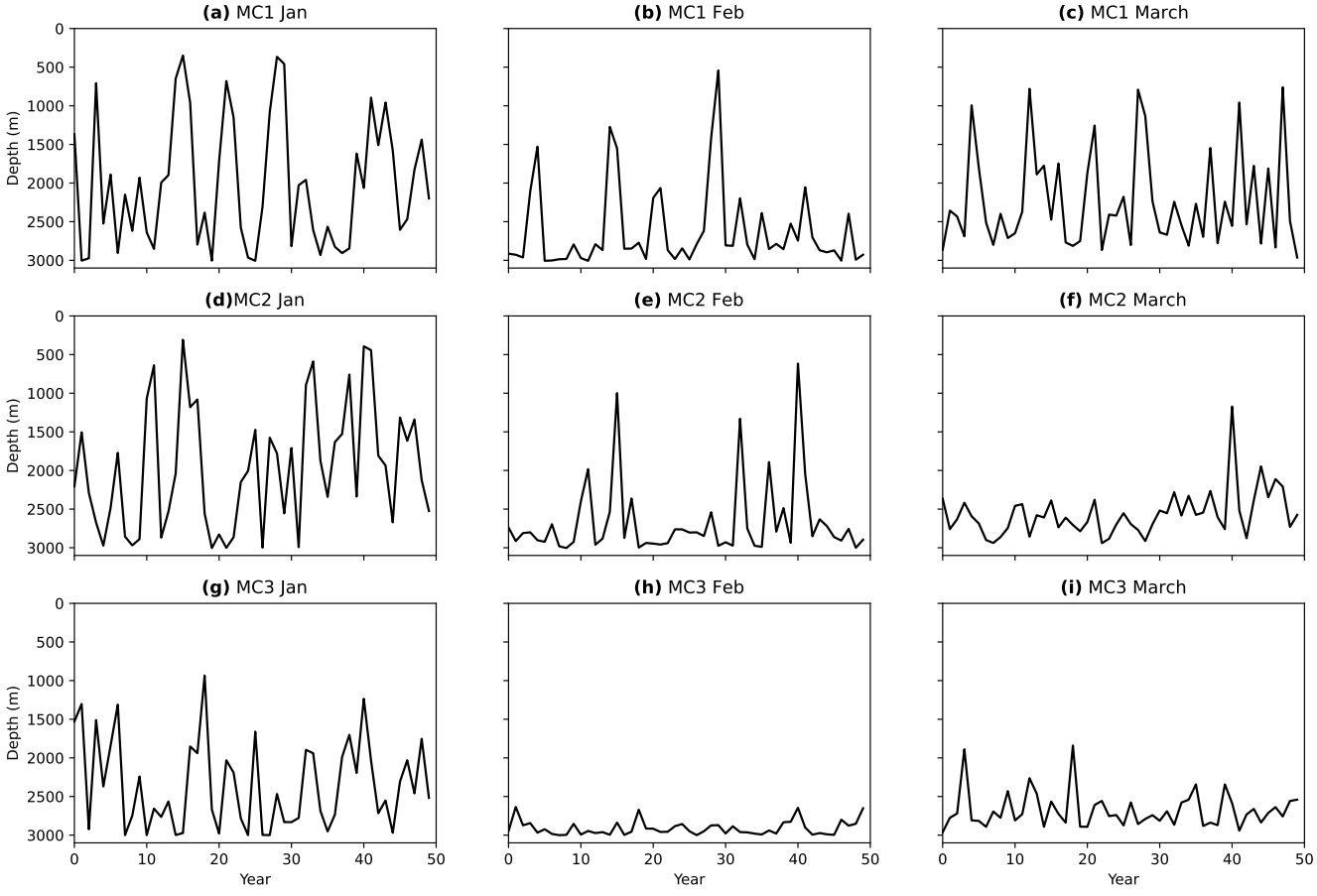

Figure A8. Timeseries of the maximum monthly average mixed layer depth in the Tethys Sea for the 50 year analysis period in January (left column), February (middle column) and March (right column) for MC1 (top row), MC2 (middle row) and MC3 (bottom row) simulations.

https://doi.org/10.5194/egusphere-2026-3378
Preprint. Discussion started: 1 July 2026

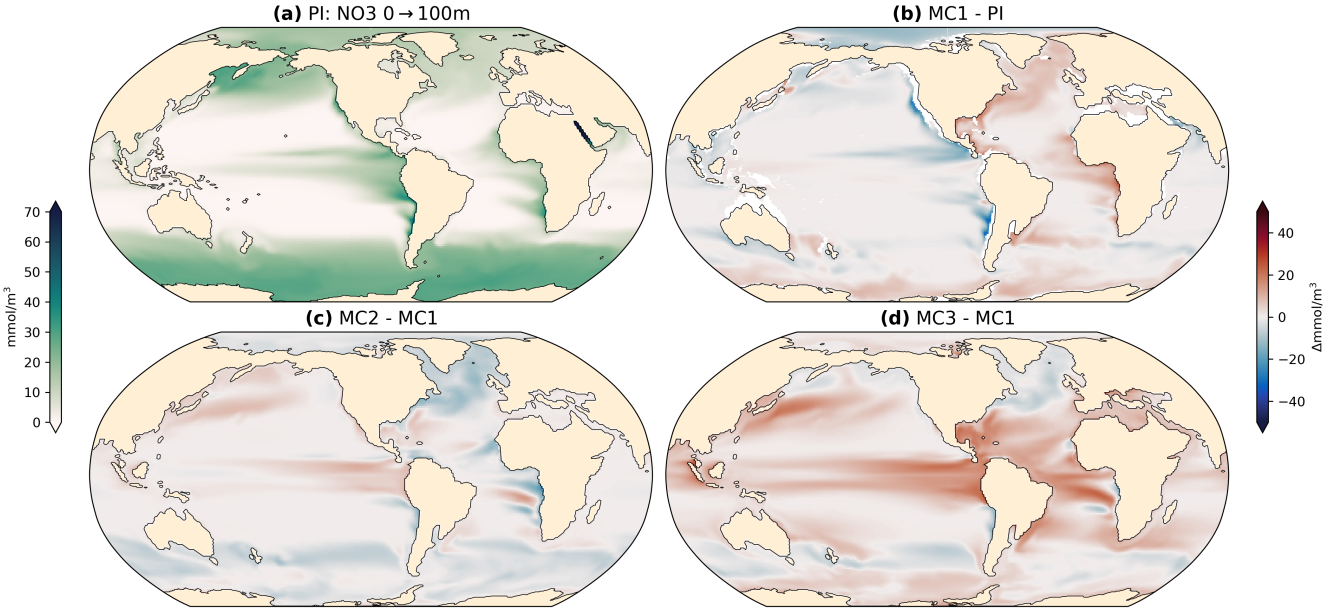

Figure A9. NO_3 averaged between 0 and 100 m for PI (a), and NO_3 anomalies for MC1 - PI (b), MC2 - MC1 (c) and MC3 - MC1 (d).

https://doi.org/10.5194/egusphere-2026-3378
Preprint. Discussion started: 1 July 2026

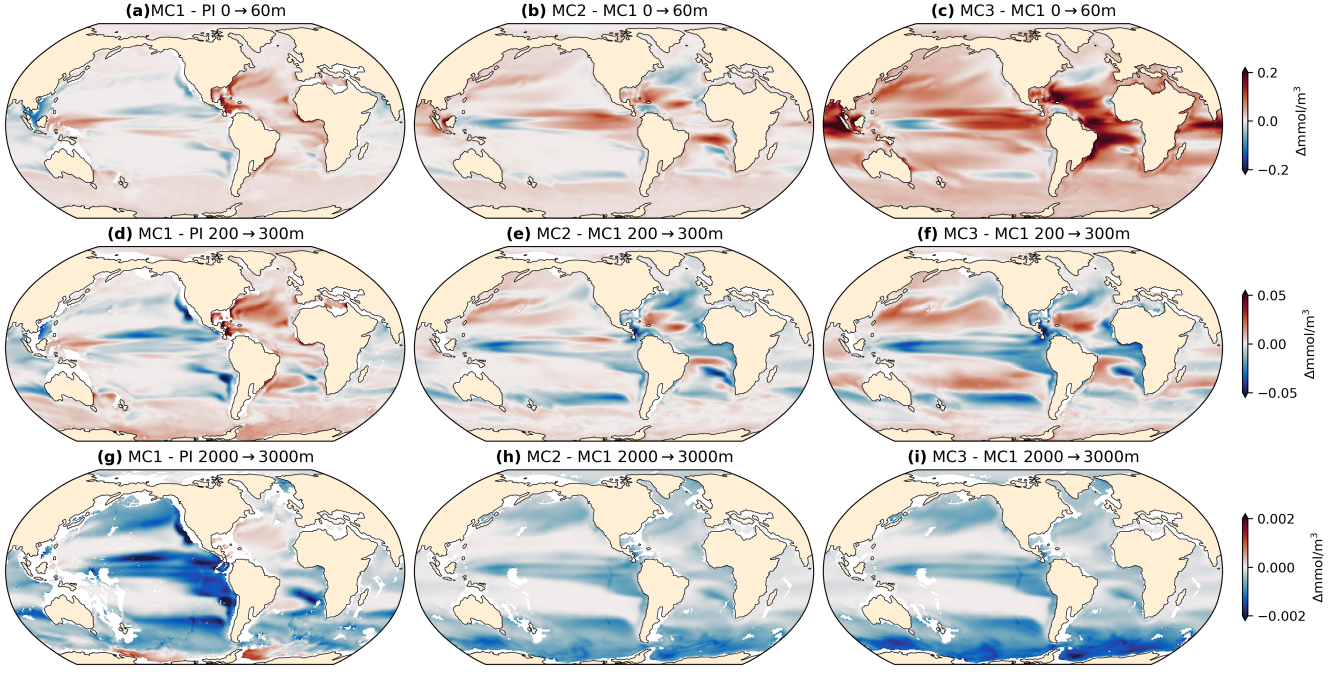

Figure A10. Detrital nitrogen concentration anomalies between MC1 and PI simulations (first column), anomalies between MC2 and MC1 (second column) and anomalies between MC3 and MC1 (third column), averaged between 0 and 60 m (first row), between 200 and 300 m (second row) and between 2000 and 3000 m (third row). Note that the colour scale is changed between rows for clarity.

https://doi.org/10.5194/egusphere-2026-3378
Preprint. Discussion started: 1 July 2026

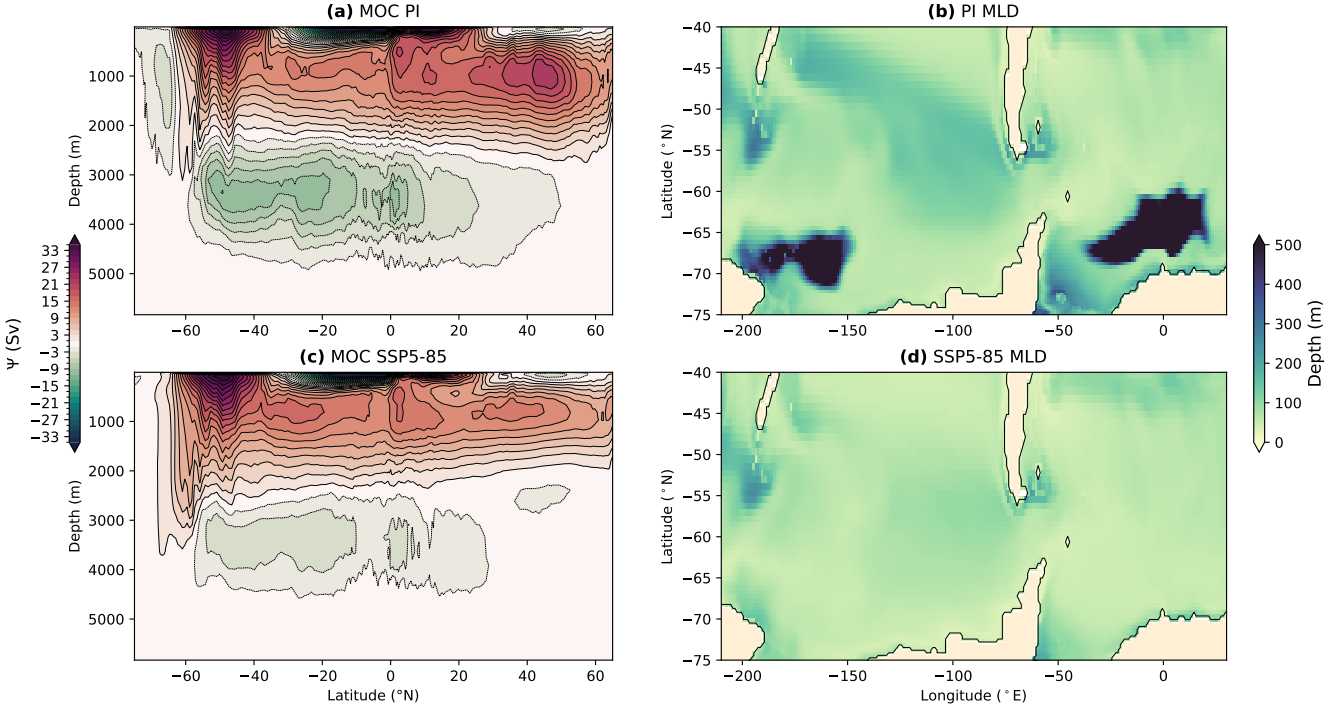

Figure A11. Meridional overturning Streamfunction for the (a) PI control experiment and (c) a high emissions scenario experiment following SSP5-8.5 forcing over years 2090-2100. Annually averaged mixed layer depth in in the Ross and Weddell seas for the PI simulation (b) and SSP5-85 (d).

https://doi.org/10.5194/egusphere-2026-3378
Preprint. Discussion started: 1 July 2026

Author contributions. Conceptualisation: David K. Hutchinson, Katrin J. Meissner
Data curation: Benjamin W. Anthonisz, David K. Hutchinson
Formal analysis: Benjamin W. Anthonisz
Funding acquisition: David K. Hutchinson, Katrin J. Meissner
Investigation: Benjamin W. Anthonisz
Methodology: David K. Hutchinson, Benjamin W. Anthonisz
Supervision: David K. Hutchinson, Katrin J. Meissner
Visualisation: Benjamin W. Anthonisz
Writing (original draft preparation): Benjamin W. Anthonisz
Writing (review and editing): Benjamin W. Anthonisz, David K. Hutchinson, Katrin J. Meissner, Benoît Pasquier, Samar Khatiwala

Competing interests. The authors declare no competing interests

Acknowledgements. BWA was supported by a Climate Change Research Centre Honours scholarship, DKH's DECRA funds and KJM's Silverstar grant. DKH acknowledges funding from the Australian Research Council (DE220100279) and KJM is grateful for funding via a UNSW Faculty of Science's Silverstar Award. BP acknowledges funding from the Australian Research Council grant SR200100008 to the Australian Centre for Excellence in Antarctic Science (ACEAS). SK was supported by UK NERC grant NE/W004976/1 as part of the Agile Initiative at the Oxford Martin School, and Waseda University's Global Research Center (GRC) Support Program (Project No. GRC-kojin-2503). This study was undertaken in collaboration with PO2, a working group of the Past Global Changes (PAGES) project, which in turn received support from the Swiss and Chinese Academies of Sciences. This research was supported by the Australian Government's National Collaborative Research Infrastructure Strategy (NCRIS), with access to computational resources provided by the National Computational Infrastructure (NCI) through the National Computational Merit Allocation Scheme (NCMAS) and the UNSW HPC at NCI scheme (https://doi.org/10.26190/PMN5-7J50).

https://doi.org/10.5194/egusphere-2026-3378
Preprint. Discussion started: 1 July 2026

References

Anderson, D. G.: Iterative Procedures for Nonlinear Integral Equations, J. ACM, 12, 547–560, https://doi.org/10.1145/321296.321305, 1965.

Anthonisz, B. W.: Honours-Analysis, https://github.com/benjWA/Honours-Analysis, 2025.

Arias, P., Bellouin, N., Coppola, E., Jones, R., Krinner, G., Marotzke, J., Naik, V., Palmer, M., Plattner, G.-K., Rogelj, J., Rojas, M., Sillmann, J., Storelvmo, T., Thorne, P., Trewin, B., Achuta Rao, K., Adhikary, B., Allan, R., Armour, K., Bala, G., Barimalala, R., Berger, S., Canadell, J., Cassou, C., Cherchi, A., Collins, W., Collins, W., Connors, S., Corti, S., Cruz, F., Dentener, F., Dereczynski, C., Di Luca, A., Diongue Niang, A., Doblas-Reyes, F., Dosio, A., Douville, H., Engelbrecht, F., Eyring, V., Fischer, E., Forster, P., Fox-Kemper, B., Fuglestvedt, J., Fyfe, J., Gillett, N., Goldfarb, L., Gorodetskaya, I., Gutierrez, J., Hamdi, R., Hawkins, E., Hewitt, H., Hope, P., Islam, A., Jones, C., Kaufman, D., Kopp, R., Kosaka, Y., Kossin, J., Krakovska, S., Lee, J.-Y., Li, J., Mauritsen, T., Maycock, T., Meinshausen, M., Min, S.-K., Monteiro, P., Ngo-Duc, T., Otto, F., Pinto, I., Pirani, A., Raghavan, K., Ranasinghe, R., Ruane, A., Ruiz, L., Sallée, J.-B., Samset, B., Sathyendranath, S., Seneviratne, S., Sörensson, A., Szopa, S., Takayabu, I., Tréguier, A.-M., van den Hurk, B., Vautard, R., von Schuckmann, K., Zaehle, S., Zhang, X., and Zickfeld, K.: Technical Summary, p. 33-144, Cambridge University Press, Cambridge, United Kingdom and New York, NY, USA, https://doi.org/10.1017/9781009157896.002, 2021.

Breitburg, D., Levin, L. A., Oschlies, A., Grégoire, M., Chavez, F. P., Conley, D. J., Garçon, V., Gilbert, D., Gutiérrez, D., Isensee, K., Jacinto, G. S., Limburg, K. E., Montes, I., Naqvi, S. W. A., Pitcher, G. C., Rabalais, N. N., Roman, M. R., Rose, K. A., Seibel, B. A., Telszewski, M., Yasuhara, M., and Zhang, J.: Declining oxygen in the global ocean and coastal waters, Science, 359, eaam7240, https://doi.org/10.1126/science.aam7240, publisher: American Association for the Advancement of Science, 2018.

Buchanan, P. J., Reddy, P. J., Matear, R. J., Chamberlain, M. A., Rohr, T., Squire, D., and Shadwick, E. H.: Optimisation of the World Ocean Model of Biogeochemistry and Trophic-dynamics (WOMBAT) using surrogate machine learning methods, EGUsphere, pp. 1–61, https://doi.org/10.5194/egusphere-2024-4026, publisher: Copernicus GmbH, 2025.

Buchanan, P. J., Squire, D., Jayasuriya, H., Gatti, T., Gálvez Vallejo, J. L., Aslekar, R., Zadeh, N., Krasting, J., Paulot, F., Underwood, S., Ross, A., Hallberg, R., Menzel, R., Stock, C., Robinson, T., and Harrison, M.: ACCESS-NRI fork of GFDL generic tracers, including the WOMBAT ocean biogeochemistry models, https://github.com/ACCESS-NRI/GFDL-generic-tracers, 2026.

Burls, N. and Sagoo, N.: Increasingly Sophisticated Climate Models Need the Out-Of-Sample Tests Paleoclimates Provide, Journal of Advances in Modeling Earth Systems, 14, e2022MS003 389, https://doi.org/10.1029/2022MS003389, _eprint: https://agupubs.onlinelibrary.wiley.com/doi/pdf/10.1029/2022MS003389, 2022.

Burls, N. J., Bradshaw, C. D., De Boer, A. M., Herold, N., Huber, M., Pound, M., Donnadieu, Y., Farnsworth, A., Frigola, A., Gasson, E., von der Heydt, A. S., Hutchinson, D. K., Knorr, G., Lawrence, K. T., Lear, C. H., Li, X., Lohmann, G., Lunt, D. J., Marzocchi, A., Prange, M., Riihimaki, C. A., Sarr, A.-C., Siler, N., and Zhang, Z.: Simulating Miocene Warmth: Insights From an Opportunistic Multi-Model Ensemble (MioMIP1), 36, e2020PA004 054, https://doi.org/10.1029/2020PA004054, _eprint: https://onlinelibrary.wiley.com/doi/pdf/10.1029/2020PA004054, 2021.

Cui, Q., Zhang, J., Hu, Y., Flögel, S., Guo, H., and Chen, Y.: Transient modeling for ocean redox conditions during the mid-cretaceous Oceanic Anoxic Event 2, Global and Planetary Change, 253, 104 976, https://doi.org/10.1016/j.gloplacha.2025.104976, 2025.

Drijfhout, S., Angevaare, J. R., Mecking, J., van Westen, R. M., and Rahmstorf, S.: Shutdown of northern Atlantic overturning after 2100 following deep mixing collapse in CMIP6 projections, Environmental Research Letters, 20, 094 062, https://doi.org/10.1088/1748-9326/adfa3b, 2025.

https://doi.org/10.5194/egusphere-2026-3378
Preprint. Discussion started: 1 July 2026

Duboc, B., Meissner, K. J., Menviel, L., Yeung, N. K. H., Hoogakker, B., Ziehn, T., and Chamberlain, M.: Simulated ocean oxygenation during the interglacials MIS 5e and MIS 9e, EGUsphere, pp. 1–38, https://doi.org/10.5194/egusphere-2024-2675, publisher: Copernicus GmbH, 2024.

Ferreira, D., Cessi, P., Coxall, H. K., De Boer, A., Dijkstra, H. A., Drijfhout, S. S., Eldevik, T., Harnik, N., McManus, J. F., Marshall, D. P., Nilsson, J., Roquet, F., Schneider, T., and Wills, R. C.: Atlantic-Pacific Asymmetry in Deep Water Formation, Annual Review of Earth and Planetary Sciences, 46, 327–352, https://doi.org/10.1146/annurev-earth-082517-010045, 2018.

Gérard, J., Sablon, L., Huygh, J. J. C., Da Silva, A.-C., Pohl, A., Vérard, C., and Crucifix, M.: Exploring the mechanisms of Devonian oceanic anoxia: impact of ocean dynamics, palaeogeography, and orbital forcing, Climate of the Past, 21, 239–260, https://doi.org/10.5194/cp-21-239-2025, 2025.

Herbert, T. D., Dalton, C. A., Liu, Z., Salazar, A., Si, W., and Wilson, D. S.: Tectonic degassing drove global temperature trends since 20 Ma, Science, 377, 116–119, https://doi.org/10.1126/science.abl4353, publisher: American Association for the Advancement of Science, 2022.

Hossain, A., Knorr, G., Jokat, W., Lohmann, G., Hochmuth, K., Gierz, P., Gohl, K., and Stepanek, C.: The Impact of Different Atmospheric CO2 Concentrations on Large Scale Miocene Temperature Signatures, Paleoceanography and Paleoclimatology, 38, e2022PA004 438, https://doi.org/10.1029/2022PA004438, _eprint: https://onlinelibrary.wiley.com/doi/pdf/10.1029/2022PA004438, 2023.

Hutchinson, D.: dkhutch/access_esm_miocene, https://github.com/dkhutch/access_esm_miocene, original-date: 2023-10-27T02:54:58Z, 2023.

Hutchinson, D. K., de Boer, A. M., Coxall, H. K., Caballero, R., Nilsson, J., and Baatsen, M.: Climate sensitivity and meridional overturning circulation in the late Eocene using GFDL CM2.1, Climate of the Past, 14, 789–810, https://doi.org/10.5194/cp-14-789-2018, 2018.

Hutchinson, D. K., Coxall, H. K., ORegan, M., Nilsson, J., Caballero, R., and de Boer, A. M.: Arctic closure as a trigger for Atlantic overturning at the Eocene-Oligocene Transition, Nature Communications, 10, 3797, https://doi.org/10.1038/s41467-019-11828-z, 2019.

Hutchinson, D. K., Meissner, K. J., Menviel, L., Wright, N. M., Berg, J., and Acosta, R. P.: Pacific and Atlantic Modes of Overturning in the Miocene Climatic Optimum, Paleoceanography and Paleoclimatology, 40, e2025PA005 220, https://doi.org/10.1029/2025PA005220, _eprint: https://agupubs.onlinelibrary.wiley.com/doi/pdf/10.1029/2025PA005220, 2025.

Kemp, A. E. S. and Villareal, T. A.: High diatom production and export in stratified waters – A potential negative feedback to global warming, Progress in Oceanography, 119, 4–23, https://doi.org/10.1016/j.pocean.2013.06.004, 2013.

Khatiwala, S.: Fast Spin-Up of Geochemical Tracers in Ocean Circulation and Climate Models, Journal of Advances in Modeling Earth Systems, 15, e2022MS003 447, https://doi.org/10.1029/2022MS003447, _eprint: https://onlinelibrary.wiley.com/doi/pdf/10.1029/2022MS003447, 2023.

Khatiwala, S.: Efficient spin-up of Earth System Models using sequence acceleration, https://www.youtube.com/watch?v=fU_Ey5haF_M, 2024.

Kvale, K. F., Meissner, K. J., and Keller, D. P.: Potential increasing dominance of heterotrophy in the global ocean, Environmental Research Letters, 10, 074 009, https://doi.org/10.1088/1748-9326/10/7/074009, 2015.

Lago, V. and England, M. H.: Projected Slowdown of Antarctic Bottom Water Formation in Response to Amplified Meltwater Contributions, https://doi.org/10.1175/JCLI-D-18-0622.1, 2019.

Law, R. M., Ziehn, T., Matear, R. J., Lenton, A., Chamberlain, M. A., Stevens, L. E., Wang, Y.-P., Srbinovsky, J., Bi, D., Yan, H., and Vohralik, P. F.: The carbon cycle in the Australian Community Climate and Earth System Simulator (ACCESS-ESM1) – Part 1: Model description and pre-industrial simulation, 10, 2567–2590, https://doi.org/10.5194/gmd-10-2567-2017, publisher: Copernicus GmbH, 2017.

https://doi.org/10.5194/egusphere-2026-3378
Preprint. Discussion started: 1 July 2026

Lee, D., Sarr, A.-C., Acosta, R. P., and Poulsen, C. J.: Multiple Ocean Equilibria and Decoupling of Miocene Atmospheric pCO2 and Regional Temperatures, Paleoceanography and Paleoclimatology, 40, e2025PA005 126, https://doi.org/10.1029/2025PA005126, _eprint: https://agupubs.onlinelibrary.wiley.com/doi/pdf/10.1029/2025PA005126, 2025.

Liu, X., Herold, N., and Huber, M.: Atlantic Meridional Overturning Circulation Influence on the Annual Mean Intertropical Convergence Zone Location in the Miocene, Geophysical Research Letters, 51, e2024GL109 159, https://doi.org/10.1029/2024GL109159, _eprint: https://agupubs.onlinelibrary.wiley.com/doi/pdf/10.1029/2024GL109159, 2024.

Mackallah, C., Chamberlain, M. A., Law, R. M., Dix, M., Ziehn, T., Bi, D., Bodman, R., Brown, J. R., Dobrohotoff, P., Druken, K., Evans, B., Harman, I. N., Hayashida, H., Holmes, R., Kiss, A. E., Lenton, A., Liu, Y., Marsland, S., Meissner, K., Menviel, L., O'Farrell, S., Rashid, H. A., Ridzwan, S., Savita, A., Srbinovsky, J., Sullivan, A., Trenham, C., Vohralik, P. F., Wang, Y.-P., Williams, G., Woodhouse, M. T., and Yeung, N.: ACCESS datasets for CMIP6: methodology and idealised experiments, Journal of Southern Hemisphere Earth Systems Science, 72, 93–116, https://doi.org/10.1071/ES21031, 2022.

Mancini, A. M., Lozar, F., Gennari, R., Capozzi, R., Morigi, C., and Negri, A.: The past to unravel the future: Deoxygenation events in the geological archive and the anthropocene oxygen crisis, Earth-Science Reviews, 249, 104 664, https://doi.org/10.1016/j.earscirev.2023.104664, 2024.

Meissner, K. J., Eby, M., Weaver, A. J., and Saenko, O. A.: CO2 threshold for millennial-scale oscillations in the climate system: implications for global warming scenarios, Climate Dynamics, 30, 161–174, https://doi.org/10.1007/s00382-007-0279-0, 2008.

Naik, T. J., de Boer, A. M., Coxall, H. K., Burls, N. J., Bradshaw, C. D., Donnadieu, Y., Farnsworth, A., Frigola, A., Herold, N., Huber, M., Karami, M. P., Knorr, G., LeGrande, A. N., Li, Y., Lohmann, G., Lunt, D. J., Prange, M., and Zhang, Y.: Ocean Meridional Overturning Circulation During the Early and Middle Miocene, Paleoceanography and Paleoclimatology, 40, e2024PA005 055, https://doi.org/10.1029/2024PA005055, _eprint: https://agupubs.onlinelibrary.wiley.com/doi/pdf/10.1029/2024PA005055, 2025.

Oke, P. R., Griffin, D. A., Schiller, A., Matear, R. J., Fiedler, R., Mansbridge, J., Lenton, A., Cahill, M., Chamberlain, M. A., and Ridgway, K.: Evaluation of a near-global eddy-resolving ocean model, Geoscientific Model Development, 6, 591–615, https://doi.org/10.5194/gmd-6-591-2013, publisher: Copernicus GmbH, 2013.

Oschlies, A., Duteil, O., Getzlaff, J., Koeve, W., Landolfi, A., and Schmidtko, S.: Patterns of deoxygenation: sensitivity to natural and anthropogenic drivers, 375, 20160 325, https://doi.org/10.1098/rsta.2016.0325, publisher: Royal Society, 2017.

Pasquier, B., Matear, R. J., Chamberlain, M. A., Ziehn, T., Hutchinson, D. K., Primeau, F. W., Liu, Y., and Bardin, A.: The Sequestration Efficiency of the Deep Ocean, Geophysical Research Letters, 52, e2025GL116 799, https://doi.org/10.1029/2025GL116799, _eprint: https://agupubs.onlinelibrary.wiley.com/doi/pdf/10.1029/2025GL116799, 2025.

Pohl, A., Ridgwell, A., Stockey, R., Thomazo, C., Keane, A., Vennin, E., and Scotese, C.: Continental configuration controls ocean oxygenation during the Phanerozoic, Nature, 608, 523–527, https://doi.org/10.1038/s41586-022-05018-z, 2022.

Rae, J. W. B., Zhang, Y. G., Liu, X., Foster, G. L., Stoll, H. M., and Whiteford, R. D. M.: Atmospheric CO2 over the Past 66 Million Years from Marine Archives, Annual Review of Earth and Planetary Sciences, 49, 609–641, https://doi.org/10.1146/annurev-earth-082420-063026, publisher: Annual Reviews, 2021.

Rampino, M. R., Caldeira, K., and Rodriguez, S.: Cycles of ∼32.5 My and ∼26.2 My in correlated episodes of continental flood basalts (CFBs), hyper-thermal climate pulses, anoxic oceans, and mass extinctions over the last 260 My: Connections between geological and astronomical cycles, Earth-Science Reviews, 246, 104 548, https://doi.org/10.1016/j.earscirev.2023.104548, 2023.

https://doi.org/10.5194/egusphere-2026-3378
Preprint. Discussion started: 1 July 2026

Shepherd, J. G., Brewer, P. G., Oschlies, A., and Watson, A. J.: Ocean ventilation and deoxygenation in a warming world: introduction and overview, Philosophical Transactions of the Royal Society A: Mathematical, Physical and Engineering Sciences, 375, 20170 240, https://doi.org/10.1098/rsta.2017.0240, publisher: Royal Society, 2017.

Sooraj, C. P., Gupta, S., and Punekar, J.: Spatio-temporal variability in microfossil and geochemical records of Cenomanian-Turonian oceanic anoxic event-2: a review, Journal of Palaeogeography, 13, 646–674, https://doi.org/10.1016/j.jop.2024.06.002, 2024.

Steinthorsdottir, M., Coxall, H. K., de Boer, A. M., Huber, M., Barbolini, N., Bradshaw, C. D., Burls, N. J., Feakins, S. J., Gasson, E., Henderiks, J., Holbourn, A. E., Kiel, S., Kohn, M. J., Knorr, G., Kürschner, W. M., Lear, C. H., Liebrand, D., Lunt, D. J., Mörs, T., Pearson, P. N., Pound, M. J., Stoll, H., and Strömberg, C. a. E.: The Miocene: The Future of the Past, Paleoceanography and Paleoclimatology, 36, e2020PA004 037, https://doi.org/10.1029/2020PA004037, _eprint: https://onlinelibrary.wiley.com/doi/pdf/10.1029/2020PA004037, 2021a.

Steinthorsdottir, M., Jardine, P. E., and Rember, W. C.: Near-Future pCO2 During the Hot Miocene Climatic Optimum, Paleoceanography and Paleoclimatology, 36, e2020PA003 900, https://doi.org/10.1029/2020PA003900, _eprint: https://onlinelibrary.wiley.com/doi/pdf/10.1029/2020PA003900, 2021b.

Stramma, L., Johnson, G. C., Sprintall, J., and Mohrholz, V.: Expanding Oxygen-Minimum Zones in the Tropical Oceans, Science, 320, 655–658, https://doi.org/10.1126/science.1153847, publisher: American Association for the Advancement of Science, 2008.

Takano, Y., Ilyina, T., Tjiputra, J., Eddebbar, Y. A., Berthet, S., Bopp, L., Buitenhuis, E., Butenschön, M., Christian, J. R., Dunne, J. P., Gröger, M., Hayashida, H., Hieronymus, J., Koenigk, T., Krasting, J. P., Long, M. C., Lovato, T., Nakano, H., Palmieri, J., Schwinger, J., Séférian, R., Suntharalingam, P., Tatebe, H., Tsujino, H., Urakawa, S., Watanabe, M., and Yool, A.: Simulations of ocean deoxygenation in the historical era: insights from forced and coupled models, Frontiers in Marine Science, 10, https://doi.org/10.3389/fmars.2023.1139917, publisher: Frontiers, 2023.

Tan, N., Fluteau, F., Zhang, Z., Ramstein, G., Guo, C., Sepulchre, P., He, Z., Zhang, Z., and Guo, Z.: A critical role of ocean–sea ice interactions in the pronounced warmth during the Miocene Climatic Optimum, Communications Earth & Environment, 7, 326, https://doi.org/10.1038/s43247-026-03324-2, 2026.

Yeung, N. K.-H., Menviel, L., Meissner, K. J., Choudhury, D., Ziehn, T., and Chamberlain, M. A.: Last Interglacial subsurface warming on the Antarctic shelf triggered by reduced deep-ocean convection, Communications Earth & Environment, 5, 212, https://doi.org/10.1038/s43247-024-01383-x, 2024.

Yool, A., Palmiéri, J., Jones, C. G., Sellar, A. A., de Mora, L., Kuhlbrodt, T., Popova, E. E., Mulcahy, J. P., Wiltshire, A., Rumbold, S. T., Stringer, M., Hill, R. S. R., Tang, Y., Walton, J., Blaker, A., Nurser, A. J. G., Coward, A. C., Hirschi, J., Woodward, S., Kelley, D. I., Ellis, R., and Rumbold-Jones, S.: Spin-up of UK Earth System Model 1 (UKESM1) for CMIP6, Journal of Advances in Modeling Earth Systems, 12, e2019MS001 933, https://doi.org/10.1029/2019MS001933, _eprint: https://onlinelibrary.wiley.com/doi/pdf/10.1029/2019MS001933, 2020.

Zhu, F. and Rose, B. E. J.: Unforced Millennial-Scale Oscillations in a Coupled Climate–Carbon System, Journal of Climate, https://doi.org/10.1175/JCLI-D-23-0762.1, section: Journal of Climate, 2025.

Zhu, J., Poulsen, C. J., and Tierney, J. E.: Simulation of Eocene extreme warmth and high climate sensitivity through cloud feedbacks, Science Advances, 5, eaax1874, https://doi.org/10.1126/sciadv.aax1874, 2019.

Ziehn, T., Chamberlain, M., Law, R., Lenton, A., Bodman, R., Dix, M., Stevens, L., Wang, Y.-P., and Srbinovsky, J.: The Australian Earth System Model: ACCESS-ESM1.5, Journal of Southern Hemisphere Earth Systems Science, 70, 193–214, https://doi.org/10.1071/ES19035, 2020.